



Mass transport at gas-evolving electrodes

Farzan Sepahi^{1,†}, Roberto Verzicco^{1,2,3}, Detlef Lohse^{1,4} and Dominik Krug^{1,†}

¹Physics of Fluids group, Max Planck Center for Complex Fluid Dynamics, and J. M. Burgers Centre for Fluid Dynamics, University of Twente, P.O. Box 217, 7500AE Enschede, Netherlands

²Dipartimento di Ingegneria Industriale, University of Rome 'Tor Vergata', Via del Politecnico 1, Roma 00133, Italy

³Gran Sacco Science Institute – Viale F. Crispi, 7 67100 L'Aquila, Italy

⁴Max Planck Institute for Dynamics and Self-Organization, Am Fassberg 17, 37077 Göttingen, Germany

(Received 19 October 2023; revised 5 December 2023; accepted 3 January 2024)

Direct numerical simulations are utilised to investigate mass-transfer processes at gas-evolving electrodes that experience successive formation and detachment of bubbles. The gas–liquid interface is modelled employing an immersed boundary method. We simulate the growth phase of the bubbles followed by their departure from the electrode surface in order to study the mixing induced by these processes. We find that the growth of the bubbles switches from a diffusion-limited mode at low to moderate fractional bubble coverages of the electrode to a reaction-limited growth dynamics at high coverages. Furthermore, our results indicate that the net transport within the system is governed by the effective buoyancy driving induced by the rising bubbles and that mechanisms commonly subsumed under the term ‘microconvection’ do not significantly affect the mass transport. Consequently, the resulting gas transport for different bubble sizes, current densities and electrode coverages can be collapsed onto one single curve and only depends on an effective Grashof number. The same holds for the mixing of the electrolyte when additionally taking the effect of surface blockage by attached bubbles into account. For the gas transport to the bubble, we find that the relevant Sherwood numbers also collapse onto a single curve when accounting for the driving force of bubble growth, incorporated in an effective Jakob number. Finally, linking the hydrogen transfer rates at the electrode and the bubble interface, an approximate correlation for the gas-evolution efficiency has been established. Taken together, these findings enable us to deduce parametrisations for all response parameters of the systems.

Key words: bubble dynamics, multiphase flow

† Email addresses for correspondence: f.sepahi@utwente.nl, d.j.krug@utwente.nl

© The Author(s), 2024. Published by Cambridge University Press. This is an Open Access article, distributed under the terms of the Creative Commons Attribution-NonCommercial-NoDerivatives licence (<http://creativecommons.org/licenses/by-nc-nd/4.0>), which permits non-commercial re-use, distribution, and reproduction in any medium, provided that no alterations are made and the original article is properly cited. The written permission of Cambridge University Press must be obtained prior to any commercial use and/or adaptation of the article.

1. Introduction

Production of green hydrogen through water electrolysis is projected to be an important technology to cope with the volatile output from renewable power sources in the future energy mix and as a sustainable feedstock in various industrial processes (Turner 2004; Holladay *et al.* 2009; Nikolaidis & Poullikkas 2017; Dawood, Anda & Shafiullah 2020). For the required upscaling of the production, the formation of gas bubbles on the electrode surface plays a critical role. Attached bubbles lower the efficiency of the electrolyser systems by blocking the active electrode area (Qian, Chen & Chen 1998; Vogt & Balzer 2005; Swiegers *et al.* 2021). In addition, they increase the cell resistance by lowering the effective conductivity of the electrolyte (Dukovic & Tobias 1987; Darband, Aliofkhaezai & Shanmugam 2019; Zhao, Ren & Luo 2019), which leads to cell overpotential. However, the formation of bubbles is also beneficial as it enhances the mixing of the electrolyte and this aspect will be the main focus of this work.

The evolution of bubbles comprises nucleation, growth and detachment from the electrode surface. Bubble growth occurs due to the diffusive transport of dissolved hydrogen to the gas–liquid interface and its subsequent desorption to the gas phase (Roušar & Cezner 1975; Angulo *et al.* 2020). The eventual detachment may be buoyancy driven (Fritz 1935; Slooten 1984) but can also be a consequence of coalescence events (Iwata *et al.* 2022). Bubble evolution can impact mass transfer at the electrode in several ways. This includes local ‘micro-convection’ and diffusion processes induced by bubble growth and break-off from the electrode surface (Stephan & Vogt 1979; Vogt & Stephan 2015), and also ‘macro-convection’ within the bulk electrolyte caused by frequent detachment and rise of bubbles within the electrolyte solution (Janssen & Barendrecht 1979; Boissonneau & Byrne 2000; Vogt 2011*b*; Taqieddin *et al.* 2017). The latter process is also referred to as two-phase buoyancy-driven convection as it results from the density variations in gas-in-liquid dispersion, and enhances the mass transport by mixing the electrolyte solution in electrode proximity via the established macro-flow pattern. Similar to forced convection effects induced by a pressure gradient or magnetic field (Iida, Matsushima & Fukunaka 2007; Koza *et al.* 2011; Matsushima, Iida & Fukunaka 2013; Baczymalski *et al.* 2016, 2017), such a flow structure pumps the fresh bulk electrolyte to the electrode surface replacing the reactant-depleted and gas-enriched solution in the electrode boundary layer (Zuber 1963). The significance of two-phase buoyancy-driven convection is further emphasised by the fact that the efficiency of electrochemical systems reduces remarkably under the microgravity condition. This adverse effect was attributed to the prolonged adherence of the bubbles to the electrode, inhibiting proper mixing, as well as their growth to inordinate sizes, which further impeded the mass transfer to the electrode (Iwasaki *et al.* 1997; Matsushima *et al.* 2003, 2009; Mandin *et al.* 2014; Sakuma, Fukunaka & Matsushima 2014; Bashkatov *et al.* 2021).

These different mass-transfer mechanisms were studied separately in the literature. Ibl *et al.* (1971) established the first mass-transfer relation for the diffusive micro-processes associated with bubble evolution. This model neglected convection and focused on reactant diffusion to a microarea on the electrode surface that is affected during the waiting period after bubble detachment and nucleation of the subsequent one. This relation was later modified by Roušar & Cezner (1975) and Vogt & Stephan (2015) to additionally account for diffusive transport during bubble growth, when the size of the microarea shrinks over time and becomes inactive under the bubble foot.

The impact of micro-convection resulting from bubble growth on mass transfer at the microarea was first quantified by Stephan & Vogt (1979). Later, Vogt & Stephan (2015) also took the effect of the wake, which is induced by the bubble break-off, on

mass transfer at the microarea into consideration. Based on their considerations, these authors concluded that micro-convection of bubble growth and detachment is the primary controlling factor for mass transfer when the gas-evolution rate is sufficiently high, particularly at moderate and large current densities. This model is almost exclusively based on theoretical considerations, but has extensively been used for practical applications by other authors (Burdyny *et al.* 2017; Yang, Kas & Smith 2019).

In contrast to the findings of Stephan & Vogt (1979) and Vogt & Stephan (2015), who identified the micro-convective processes of gas evolution as the dominant mechanism, Janssen & Hoogland (1970, 1973), Janssen (1978) and Janssen & Barendrecht (1979) provided evidence that mass transfer at the electrode was governed by two-phase free convection driven by rising bubbles. This was corroborated by measurements conducted on hydrogen-evolving electrodes, with no coalescence of bubbles, where the boundary-layer thickness, as a function of volumetric gas-evolution rate, exhibited a power law relationship with an exponent of 1/3. This observation highlighted the analogy between such flows, induced by density variations in gas-in-liquid dispersion, and single-phase natural convection in heat and mass-transfer problems (Wragg 1968; Churchill & Chu 1975).

In summary, the findings by different authors on the relevance of the various transport processes close to the gas-producing electrodes are contradictory, and as of our current knowledge, there is no consensus on the rate-controlling mechanism, let alone a well-controlled quantification, of mass transfer at gas-evolving electrodes.

Numerous attempts have been made in the literature to combine experiments and numerical simulations to study the bubble-induced convection at gas-evolving electrodes (Hreiz *et al.* 2015a). The hydrodynamics of two-phase flow and its influence on the mass transfer and reaction rate at the electrode have been modelled employing Euler–Euler (Abdelouahed *et al.* 2014a,b; Schillings, Doche & Deseure 2015; Obata *et al.* 2020; Zarghami, Deen & Vreman 2020; Obata & Abdi 2021) or Euler–Lagrange (Mandin *et al.* 2005; Hreiz *et al.* 2015a,b; Battistella *et al.* 2018) approaches, in neither of which was the gas–liquid interface of the bubble resolved. However, only interface-resolved simulations are capable of capturing the micro-convection as a result of bubble growth and break-off. Several authors performed numerical simulations to study the dynamics of bubble growth coupled with the electrokinetics of the gas-evolution reaction at the electrode using the immersed boundary method (IBM) (Khalighi *et al.* 2023) or body-fitted grids (Higuera 2021, 2022). Other relevant dynamics of bubbles near the electrodes, such as coalescence, detachment and rising, has separately been investigated with interface-resolved simulations (Zhang, Liu & Free 2020; Torii, Kodama & Hirai 2021). However, none of these studies simultaneously treat the effect of bubble growth-induced micro-convection and two-phase buoyancy-driven convection.

Despite numerous studies targeting the interplay between two-phase hydrodynamics and electrochemical phenomena at gas-evolving electrodes, the question of whether the primary mass transfer mechanism is attributed to the micro-convective processes of bubble growth (Stephan & Vogt 1979; Vogt & Stephan 2015) or two-phase free convection of gas-in-liquid dispersion (Janssen & Barendrecht 1979) remains unsettled. Therefore, we aim to perform interface-resolved direct numerical simulations to account for the various mechanisms at play with electrolytically generated gas bubbles. In particular, we look into the successive processes of bubble growth and rise in the electrolyte solution (van der Linde *et al.* 2017; Raman *et al.* 2022) until an equilibrium state is reached, i.e. the global statistics of the system no longer varies in time. Our findings provide a broader perspective

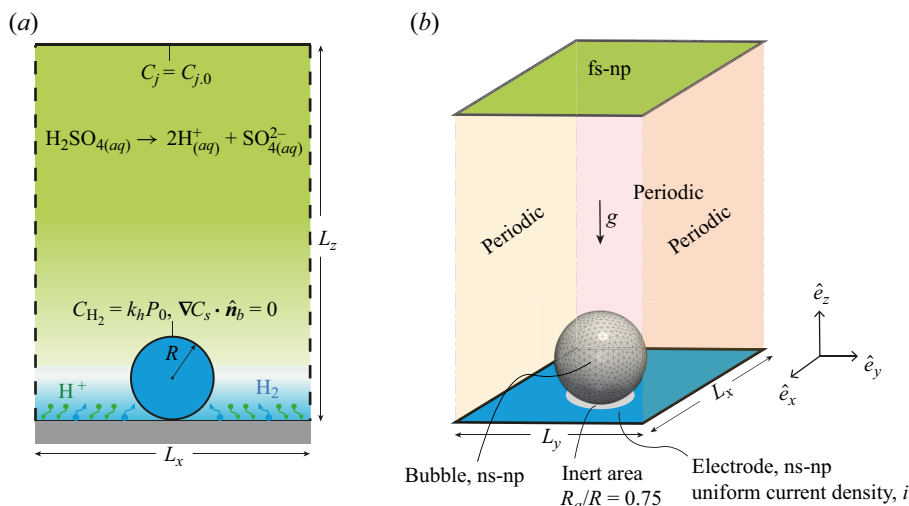


Figure 1. (a) Schematic representation of the two-phase electrochemical system with relevant chemical reactions and boundary conditions at the cathode. (b) Sketch of the three-dimensional numerical set-up with the applied boundary conditions for the velocity field (periodic, no slip (ns), no penetration (np) and free slip (fs)). The bubble is modelled with IBM using a triangulated Lagrangian grid on the bubble interface (a sample is illustrated in (b)). Current density is uniformly distributed on the electrode surface except for an inactive ($i = 0$) circular part with an outer radius of $R_a = 0.75R$ under the bubble.

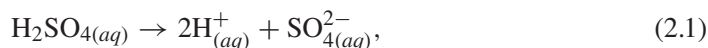
on the different mass-transfer processes at the electrode and bubble interface by leveraging disentangled parameters in the numerical simulations.

The remainder of this paper is structured as follows; the problem set-up and governing equations are discussed in § 2. The results for the bubble dynamics and mass-transfer rates at the electrode are presented in § 3. Mass transfer to the bubble and gas-evolution efficiency are quantified in §§ 4 and 5. Finally, we further discuss and summarise our findings in § 6.

2. Configuration and numerical methods

2.1. Problem set-up

The electrochemical model considered here concerns a water-splitting system with dilute sulfuric acid (H_2SO_4 , 500 mol m^{-3}) as the electrolyte. A schematic is provided in figure 1(a) demonstrating the chemical reactions at the cathodic part of the cell. Full dissociation of sulfuric acid to sulphate (SO_4^{2-}) and hydrogen (H^+) ions is assumed according to



and, in order to avoid further complications, self-ionisation of water is disregarded due to its low equilibrium constant at room temperature. The cathodic reactions solely comprise the hydrogen-evolution reaction as



whereby the hydrogen enrichment and electrolyte depletion co-occur within a mass-transfer boundary layer in the vicinity of the electrode, as schematically illustrated in figure 1(a).

Configuration				$ i $ (A m ⁻²)
Constant bubble spacing, $L_x = L_y = 2$ mm				10^1
No.	d_b (mm)	Θ	$N_x \times N_y \times N_z$	1.7×10^1
1	0.3	0.018	$144^2 \times 288$	3.0×10^1
2	0.5	0.05	$144^2 \times 288$	5.4×10^1
3	0.7	0.10	$144^2 \times 288$	10^2
4	0.9	0.16	$144^2 \times 288$	1.7×10^2
Constant bubble size, $d_b = 0.5$ mm				3.0×10^2
No.	$L_x = L_y$ (mm)	Θ	$N_x \times N_y \times N_z$	5.4×10^2
5	3	0.021	$216^2 \times 288$	1.0×10^3
6	2	0.05	$144^2 \times 288$	1.7×10^3
7	1.33	0.11	$96^2 \times 288$	3.0×10^3
8	0.89	0.25	$64^2 \times 288$	5.4×10^3
9	0.7	0.40	$48^2 \times 288$	10^4
10	0.5925	0.60	$42^2 \times 288$	

Table 1. Simulation parameters for cases with varying bubble departure diameter d_b at constant bubble spacing, and with varying bubble spacing $S = L_x = L_y$ at a fixed bubble departure diameter. The domain height is $L_z = 4$ mm for all the simulation cases. At each configuration, the simulations are performed at 13 different current densities, as listed in the last column, leading to 130 simulation cases in total.

The numerical set-up is a cuboid box, as depicted in [figure 1\(b\)](#). The electrode is oriented horizontally (x and y directions) such that the gravitational acceleration \mathbf{g} acts normal to it in the negative z direction. A fully spherical hydrogen bubble is initialised with a certain radius ($R_0 = 50 \mu\text{m}$) and zero-degree contact angle on the electrode. The bubble subsequently grows to a prescribed diameter, namely the break-off diameter d_b , before it departs from the electrode surface and rises within the electrolyte solution due to its buoyancy. This process then repeats with the next bubble initialised at the same spot as soon as the previous bubble exits from the top boundary. By applying periodicity in the lateral directions of the computational domain, the set-up replicates a system of monodisperse bubbles with uniform spacing of $S = L_x = L_y$ which synchronously grow and rise in the medium. The initialisation, growth and rise of the bubbles in succession are modelled until an equilibrium state is attained, i.e. the averaged mass-transfer statistics, which will be introduced in [§ 2.3](#), remain constant in time.

The control parameters for the electrolytically generated two-phase free-convective flow are the cathodic current density i , the bubble break-off diameter d_b and the bubble spacing S . Simulations are performed with two different sets of configurations, as listed in [table 1](#); in the first set, the bubble spacing is kept constant while the bubble break-off diameter is varied. In the second set, the spacing between the bubbles is varied at a constant break-off diameter of the bubbles to investigate the effect of bubble population density on the mass transport at the electrode. An auxiliary parameter for either set is the fractional bubble coverage of the electrode, Θ , which refers to the fraction of the electrode area shadowed by the orthogonal projection of the bubble surface. It is formulated as $\Theta = \pi d_b^2 / 4A_e$, where $A_e = L_x L_y$ is the electrode area available for a single bubble. At each configuration, 13 current densities within the range $10^1 \leq |i| \leq 10^4 \text{ A m}^{-2}$, as listed in [table 1](#), are simulated.

2.2. Governing equations

2.2.1. Carrier phase

The three-dimensional transient incompressible Navier–Stokes equations in a Cartesian coordinate system are adopted to solve for the velocity field, \mathbf{u} , which include the momentum equation

$$\frac{\partial \mathbf{u}}{\partial t} + \nabla \cdot (\mathbf{u}\mathbf{u}) = -\nabla p + \nu \nabla^2 \mathbf{u} + \mathbf{f}_u, \quad (2.3)$$

and the continuity equation

$$\nabla \cdot \mathbf{u} = 0. \quad (2.4)$$

Here, ∇ is the gradient operator vector, p is the modified kinematic pressure (i.e. the total pressure with the hydrostatic pressure subtracted) and ν is the kinematic viscosity of the solution; \mathbf{f}_u denotes the direct forcing introduced in the IBM framework in order to enforce the velocity boundary conditions on the bubble interface.

In the most general case, the distribution of the H_2SO_4 is obtained by solving the advection–diffusion–migration equation for its constituent ions (H^+ , SO_4^{2-}). However, for a binary electrolyte it is possible to simplify the problem by assuming electroneutrality throughout the electrolyte (Dickinson, Limon-Petersen & Compton 2011), thus eliminating the migration terms between the ion transport equations. Hence, a single transport equation for H_2SO_4 with an effective diffusivity is obtained (Morris & Lingane 1963; Sepahi *et al.* 2022). Additionally accounting for H_2 , the transport of each substance, C_j , in the system can be described by an effective advection–diffusion equation as

$$\frac{\partial C_j}{\partial t} + \nabla \cdot (\mathbf{u}C_j) = D_j \nabla^2 C_j + \mathbf{f}_{C_j}, \quad (2.5)$$

where the subscript $j = (s, \text{H}_2)$ refers to H_2SO_4 and H_2 , respectively. Here, \mathbf{f}_{C_j} is the IBM forcing term to enforce the respective gas–liquid interfacial condition for each substance, which will be explained in § 2.2.2. The effective diffusivity of H_2SO_4 can be obtained from the mass diffusivities, D_k , and ionic valences, z_k , of the ions ($k = 1, 2$ denotes H^+ and SO_4^{2-} , see table 2 for ions diffusivity) as

$$D_s = \frac{D_1 D_2 (z_1 - z_2)}{z_1 D_1 - z_2 D_2}. \quad (2.6)$$

The no-slip impermeable condition is applied on the electrode. A uniform current density, $i = I/A_e$, where I and A_e are respectively the overall electric current and electrode surface area, is spread on the electrode surface, except for an inactive area with instantaneous radius of $R_a = 0.75R$ (Vogt & Stephan 2015) underneath the bubble where zero current density is applied (R is the instantaneous bubble radius, see figure 1*b*). The current density in the outer region is therefore corrected slightly as the bubble grows in order to keep the overall electric current I constant throughout the simulations. The maximum transient enhancement of the local current density away from the bubble is $1/(1 - 0.75^2\Theta)$ just before the bubble departure. The current density is homogeneous across the entire electrode during the rise phase of each bubble. The cathodic set of

Symbol	Description	Value	Unit
$C_{s,0}$	H ₂ SO ₄ initial concentration	500	mol m ⁻³
$C_{H_2,0}$	H ₂ initial concentration	0	mol m ⁻³
$C_{H_2,sat}$	H ₂ saturation concentration	0.72	mol m ⁻³
T_0	Ambient temperature	298	K
P_0	Ambient pressure	1	bar
\mathcal{R}	Gas universal constant	8.314	J mol ⁻¹ K ⁻¹
ρ_L	Electrolyte density	1030	kg m ⁻³
ρ_G	H ₂ density (for simulations)	1	kg m ⁻³
μ	Electrolyte dynamic viscosity	1.03×10^{-3}	kg s ⁻¹ m ⁻¹
ν	Electrolyte kinematic viscosity	1.0×10^{-6}	m ² s ⁻¹
D_{H^+}	H ⁺ diffusivity	9.308×10^{-9}	m ² s ⁻¹
$D_{SO_4^{2-}}$	SO ₄ ²⁻ diffusivity	1.0×10^{-9}	m ² s ⁻¹
D_s	H ₂ SO ₄ diffusivity	2.47×10^{-9}	m ² s ⁻¹
D_{H_2}	H ₂ diffusivity	3.7×10^{-9}	m ² s ⁻¹
k_{h,H_2}	H ₂ Henry's constant	7.2×10^{-6}	mol m ⁻³ Pa ⁻¹

Table 2. Physical properties of the analysed system.

boundary conditions for C_j reads (Morris & Lingane 1963; Sepahi *et al.* 2022)

$$-\frac{i}{(n_e/s_1)F} = 2D_1 \left(1 - \frac{z_1}{z_2}\right) \left(\frac{\partial C_s}{\partial z}\right)_{z=0}, \quad (2.7)$$

$$\frac{i}{(n_e/s_{H_2})F} = D_{H_2} \left(\frac{\partial C_{H_2}}{\partial z}\right)_{z=0}. \quad (2.8)$$

Here, $n_e = 2$ is the number of the transferred electrons in the cathodic reaction (2.2), $s_1 = 2$ and $s_{H_2} = 1$ are the stoichiometric coefficients of the ions and $F = 96\,485 \text{ C mol}^{-1}$ is the Faraday constant. After simplification, the corresponding cathodic flux $J_j = -D_j(\partial C_j/\partial z)_{z=0}$ for each species can be related to the current density via the Faraday constant as

$$J_s = \frac{1}{3} \frac{i D_s}{F D_1}, \quad \text{and} \quad J_{H_2} = -\frac{i}{2F}. \quad (2.9a,b)$$

While generally the boundary conditions at the top boundary are free slip no penetration and constant concentrations for the velocity and scalar fields, respectively, a remedy is required to allow the bubble to pass the top boundary. For this purpose, we momentarily change the boundary condition to an in-outflow condition once the bubble arrives at the top boundary and revert back to the original boundary conditions once the bubble has left the computational box. The bubble passes through the top boundary with a constant velocity equal to its rise velocity before the boundary condition switch. We ensured that the computational domain is sufficiently high such that this procedure has negligible influence on mass-transfer processes at the electrode. Moreover, periodic boundary conditions for the velocity and concentration fields are employed in the lateral directions of the computational domain. The choice of these boundary conditions is such that the corresponding pure-diffusion problem, i.e. in the absence of advection, reaches a steady state for which an analytical self-similar solution exists (Carslaw & Jaeger 1959; van der Linde *et al.* 2017). Thus, the known mass-transfer rate of the pure-diffusion problem

can be served as a base system for comparison of the mass-transfer change resulting from the bubbly flows within the electrolyte (see § 3).

In order to numerically obtain the solution of (2.4), (2.3) and (2.5), a second-order accurate central finite-difference scheme is employed for spatial discretisation and time marching is performed with a fractional step third-order accurate Runge–Kutta scheme (Kim & Moin 1985; Verzicco & Orlandi 1996). A multiple-resolution strategy (Ostilla-Monico *et al.* 2015), with a refinement factor of two for the scalar fields, is used to solve the momentum and scalar equations, to cope with the fact that the mass diffusivity is several orders of magnitudes smaller than the momentum diffusivity. The grid is equally spaced in all directions. A grid independence check has also been performed and is reported in Appendix A.2.

2.2.2. Dispersed phase

Numerically, we represent the growth and rise phases of the bubbles but circumvent the intricacies of the nucleation process by initialising the bubbles with a finite size of $R_0 = 50 \mu\text{m}$. Effectively, the liquid previously located at the bubble position is replaced during this step. However, given the minute volume of the bubble at this point, this does not affect the results. During the growth phase, the expansion rate of the bubble is directly related to the diffusive transport of the dissolved gas across the gas–liquid interface which is determined by Fick’s law. Balancing the rate of the change of mass within the bubble and the diffusive flux of hydrogen across the interface as

$$\dot{N}_b = \frac{P_0}{\mathcal{R}T_0} 4\pi R^2 \frac{dR}{dt} = \int_{\partial V} D_{\text{H}_2} \nabla C_{\text{H}_2} \cdot \hat{\mathbf{n}}_b \, dA, \quad (2.10)$$

yields the bubble growth rate

$$\frac{dR}{dt} = \frac{\mathcal{R}T_0}{P_0} \frac{1}{4\pi R^2} \int_{\partial V} D_{\text{H}_2} \nabla C_{\text{H}_2} \cdot \hat{\mathbf{n}}_b \, dA, \quad (2.11)$$

where \mathcal{R} , T_0 and P_0 are the gas universal constant, ambient temperature and pressure, respectively. Here, R is the instantaneous radius of the bubble and $\hat{\mathbf{n}}_b$ is the unit normal vector at the surface ∂V of the bubble. We assume here a constant pressure inside the bubble throughout the growth phase, which is valid since, for the range of bubble sizes $R \geq 50 \mu\text{m}$, the Laplace pressure is negligible compared with the ambient pressure of $P_0 = 1 \text{ bar}$. We further neglected inertial effects on the pressure inside the bubble. This is confirmed to be appropriate by computing the inertial terms of Rayleigh–Plesset equation $\rho_L(R\dot{R} + 3\dot{R}^2/2)$ (Prosperetti 1982). For the largest bubble growth rates encountered in our simulations, the corresponding change in the bubble pressure does not exceed 0.2 Pa, which is small compared with P_0 .

The bubble detaches and rises under the influence of buoyancy in the electrolyte solution after growing to a prescribed departure diameter, d_b . Note that we do not consider a potential bubble growth during the rise phase such that $R = \text{const.}$ in this case. Given the short rise times ($\sim 0.1 \text{ s}$) compared with the residence time of the bubble on the electrode ($\sim 1\text{--}100 \text{ s}$) for all but the highest current densities and the significantly lower hydrogen concentrations outside the boundary layer at the electrode, this has hardly any effect on our results. The bubble is treated as a spherical rigid particle during the rising phase and its deformation is disregarded owing to its small size ($d_b < 1 \text{ mm}$), i.e. surface tension forces, which maintain the spherical form of the bubble, are predominant over inertia and drag forces in the ascent (Weber and capillary numbers are significantly lower than unity).

Mass transport at gas-evolving electrodes

We solve for the translational velocity of the bubble, \mathbf{u}_b , which we assume to be governed by Newton's second law of motion as

$$\rho_g V_b \frac{d\mathbf{u}_b}{dt} = \int_{\partial V_b} \boldsymbol{\tau} \cdot \hat{\mathbf{n}}_b dA + (\rho_G - \rho_L) V_b \mathbf{g}, \quad (2.12)$$

where

$$\mathbf{u}_b = \frac{d\mathbf{x}_b}{dt}, \quad \boldsymbol{\tau} = -p\mathbf{I} + \mu(\nabla\mathbf{u} + \nabla\mathbf{u}^T). \quad (2.13a,b)$$

Here, \mathbf{x}_b is the bubble centroid position, ρ_G and ρ_L are the gas and fluid densities, respectively, V_b is the bubble volume after detachment and $\boldsymbol{\tau}$ is the stress tensor for Newtonian fluids. A method and validation to integrate (2.12) numerically is discussed in [Appendix A.1](#).

A set of the boundary conditions for the carrier phase on the bubble interface is required for the concentration and velocity fields. Saturation concentration based on Henry's law $C_{H_2, sat} = k_h P_0$, with k_h being Henry's constant for H_2 and zero flux $\nabla C_s \cdot \hat{\mathbf{n}}_b = 0$ for H_2SO_4 , is applied on the bubble interface. Assuming a fully contaminated bubble (Takagi & Matsumoto 2011), the no-slip no-penetration condition is employed on the bubble interface ($|\mathbf{x} - \mathbf{x}_b| = R$) such that the velocity $\mathbf{u}|_{\partial V}$ of a point on the bubble surface is given by

$$\mathbf{u}|_{\partial V} = \mathbf{u}_b + \frac{dR}{dt} \hat{\mathbf{n}}_b. \quad (2.14)$$

This relation is coupled to the mass transfer via (2.11) to determine the bubble growth rate dR/dt . During the growth stage, we set $\mathbf{u}_b = dR/dt$ such that the contact point of the bubble on the electrode remains stationary. To ensure continuity within the domain during the bubble growth, the continuity equation needs to be revised by adding a source term in the bubble interior according to

$$\nabla \cdot \mathbf{u} = \phi \frac{3}{R} \frac{dR}{dt}, \quad (2.15)$$

where ϕ is an indicator function which undergoes a smooth transition from 0 to 1, based on a cut-cell method (Kempe & Fröhlich 2012) for the cells outside and inside the bubble, respectively. This amendment is necessary for modelling expanding/shrinking boundaries using an incompressible solver with IBM. The same approach has also been adopted in the literature for simulation of flows with evaporating droplets (Lupo *et al.* 2019, 2020). The local velocity field is still entirely divergence free outside the bubble and the non-zero divergence inside the bubble is irrelevant to the flow physics outside due the boundary conditions enforced on the gas–liquid interface. To ensure the global conservation of the mass in the course of the bubble growth, a small but non-zero uniform vertical velocity is prescribed at the top boundary such that the outflow rate equals the expansion rate of the bubble, similar to the simulations of evaporating droplets in wall-bounded turbulent flows using IBM (Lupo *et al.* 2020).

The bubble interface is discretised using another triangulated Lagrangian grid, as depicted in [figure 1\(b\)](#). The IBM method here is based on the moving least squares approach to conduct the interpolation and distribution of the direct forcing terms between the Eulerian and Lagrangian grids (Liu & Gu 2005; Vanella & Balaras 2009; Spandan *et al.* 2017). The enforcement of the Dirichlet and Neumann conditions on the interface for H_2 and H_2SO_4 is performed employing a ghost-cell-based IBM to ensure the conservation of the species (Lu *et al.* 2018). To validate these procedures, we verified

that mass conservation for the hydrogen distribution is fulfilled in our simulations (see Appendix A.3).

2.3. Response parameters

The most basic response parameters relate to the transport of H_2 away and H_2SO_4 towards the electrode. Since the respective rates of production and consumption at the electrode, J_{H_2} and J_s , are constant in time, the effective transport is reflected in the resulting surface-averaged concentrations of hydrogen, $\tilde{C}_{H_2,e}$, and electrolyte, $\tilde{C}_{s,e}$, at the electrode surface. These need to be compared with the respective concentration values in the bulk, for which we adopt the top boundary conditions, which equal the initial values, i.e. $C_{H_2,0} = 0$ and $C_{s,0}$. We then normalise the differences between the concentrations at the electrode and at the top of the domain using the (constant) fluxes J_j and the bubble diameter d_b as reference scales to yield the Sherwood numbers

$$\tilde{Sh}_{H_2,e} = \frac{J_{H_2}d_b}{D_{H_2}\tilde{C}_{H_2,e}} \quad \text{and} \quad \tilde{Sh}_{s,e} = \frac{J_s d_b}{D_s(C_{s,0} - \tilde{C}_{s,e})}. \quad (2.16a,b)$$

Here, and in the following, the tilde symbol is used to mark time-dependent surface-averaged response parameters; corresponding averages over a bubble period appear without a tilde. By introducing the boundary-layer thickness $\tilde{\delta}_j = D_j \Delta \tilde{C}_j / J_j$, this Sherwood number can equivalently be expressed as $\tilde{Sh}_j = d_b / \tilde{\delta}_j$. For pure diffusion, $\tilde{\delta}_j$ ultimately reaches the cell height irrespective of the current density such that the same steady-state value of \tilde{Sh}_j would be obtained for all cases without the effect of the bubbles.

Analogously, we characterise the mass transfer of hydrogen into the bubble using the bubble Sherwood number

$$\tilde{Sh}_{H_2,b} = \frac{2\dot{R}R}{\frac{\mathcal{R}T_0}{P_0}D_{H_2}(\tilde{C}_{H_2,e} - C_{H_2,sat})}, \quad (2.17)$$

which employs the instantaneous bubble diameter, $2R$, the surface area, $4\pi R^2$, and the concentration difference between the electrode and bubble interface, $(\tilde{C}_{H_2,e} - C_{H_2,sat})$, for normalisation of the mass flux into the bubble given by (2.10).

A final important output is the fraction of the total hydrogen produced that ends up in gaseous form, i.e. gets desorbed into the bubble (Vogt 1984a,b, 2011a,b). Mathematically formulating this leads to an expression for the gas-evolution efficiency

$$f_G = \frac{\frac{V_b}{\tau_c}}{\frac{\mathcal{R}T_0}{P_0} \frac{-i}{n_e F} A_e} = \frac{\dot{V}_G}{\frac{\mathcal{R}T_0}{P_0} \frac{-i}{n_e F} A_e}, \quad (2.18)$$

where $\tau_c = \tau_g + \tau_r$ is the bubble lifetime, which comprises the bubble residence (growth) time, τ_g , and the bubble rise time, τ_r . Here, $\dot{V}_G = V_b / \tau_c$ is the volumetric gas flux into the gas phase.

3. Bubble dynamics and mass transfer at the electrode

To begin with, we present the simulation results for a bubble departure diameter of $d_b = 0.5$ mm and spacing $S = 2$ mm. The physical properties of the system are set in

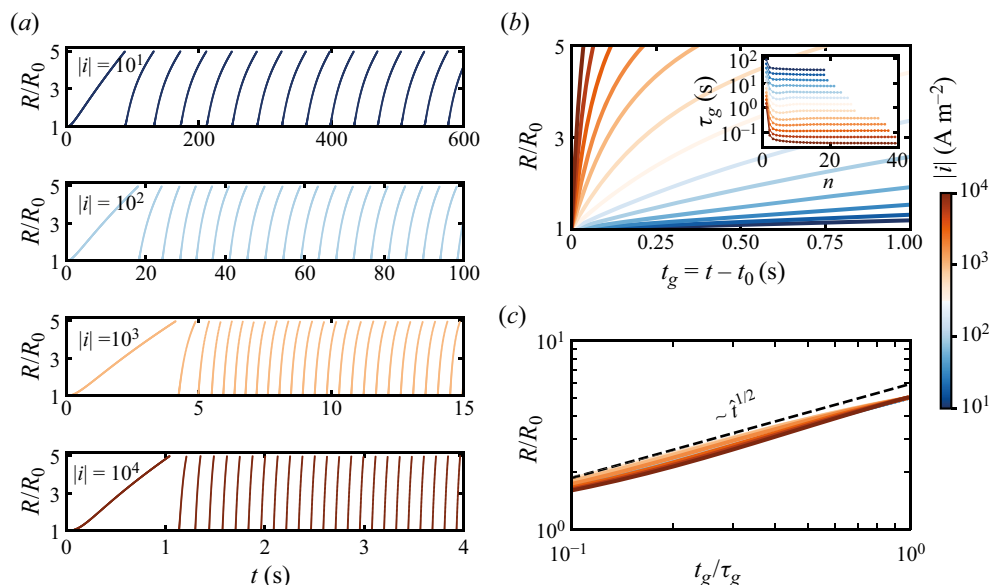


Figure 2. (a) Radius of the successively growing bubbles as a function of time for current densities $|i| = 10^1, 10^2, 10^3$ and 10^4 A m^{-2} . The radius has been normalised with the initial size of the bubble used for the simulations, $R_0 = 50 \mu\text{m}$. (b) Temporal evolution of the bubble radius at the statistically steady state for each current density in the range of $10^1 < |i| < 10^4 \text{ A m}^{-2}$. The magnitude of the current density is illustrated with the colour map. Here, t_0 is the start of the bubble lifetime in each case and hence $t_g = t - t_0$ is the bubble age. The inset shows the bubble growth time, τ_g , for the n th bubble. (c) Double-logarithmic plot of the bubble-evolution curve for all the current densities. Time axis has been normalised with the growth time in the steady state, as shown in the inset of (b).

accordance with table 2. Figure 2(a) shows the growth dynamics of successively generated bubbles on the electrode at four different current densities. At each current density, the first few bubbles show a slower growth while the supersaturation level of the gas in the electrode boundary layer is building up and the growth pattern becomes more repetitive at later times. This is also reflected in the bubble growth time, which drops initially, but remains constant for subsequent bubbles later on (see inset of figure 2b). These observations are indicative of an equilibrium state, in which the time-averaged mass transport and gas production rates at the electrode surface are balanced, leading to the repetition of the same growth dynamics for bubbles evolving in sequence. The bubble size evolution at the statistically steady state is plotted and compared in figure 2(b) for different current densities. These curves have been taken at times when the bubble residence time, τ_g , no longer varies with bubble number n , as depicted in the inset. Despite the fact that the bubble growth time varies over several orders of magnitude from 100 s to less than 0.1 s when increasing the current density from 10^1 to 10^4 A m^{-2} , the growth dynamics pertaining to diffusion-limited growth, i.e. $R \propto t^{1/2}$, is maintained (Epstein & Plesset 1950; Scriven 1959). This is evidenced by the double-logarithmic plot of the bubble size evolution in figure 2(c), where the time axis is normalised with τ_g . In this form, all cases approximately collapse onto a single curve that is in good agreement with the 1/2 power law.

Next, we look into the mass-transfer rate at the electrode by tracking the spatially averaged concentrations on the electrode surface in time, as shown in figures 3(a) and 3(b) for H_2 and H_2SO_4 , respectively. As the reaction proceeds, the hydrogen concentration

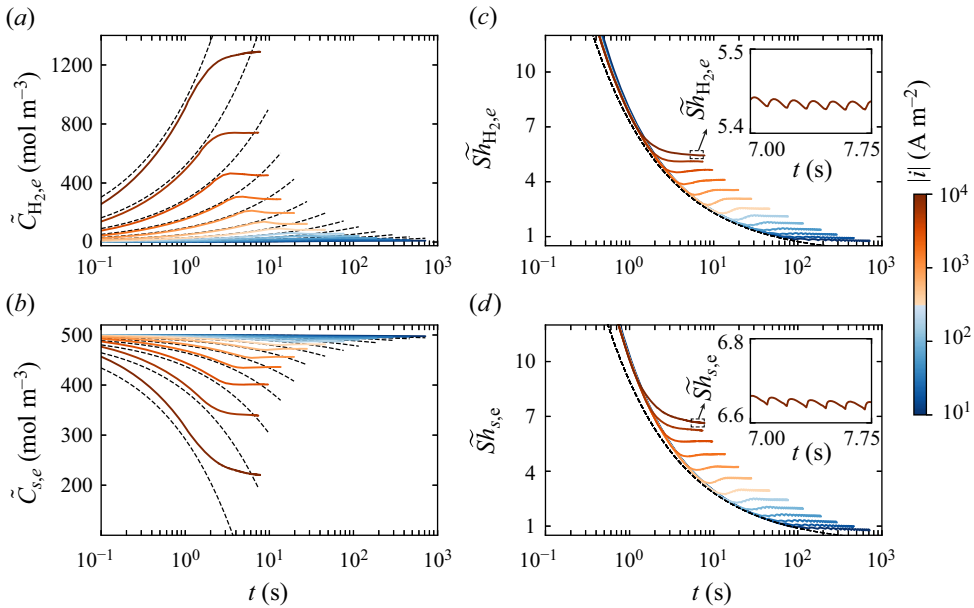


Figure 3. Temporal evolution of hydrogen (a) and electrolyte (b) averaged concentrations at the electrode surface for bubble departure diameter of $d_b = 0.5$ mm and spacing of $S = 2$ mm for all the investigated current densities. Broken black lines represent the solution of the pure-diffusion problem in a semi-infinite medium with constant flux condition at the boundary, calculated using (3.1). Corresponding Sherwood numbers of simulations and pure-diffusion problem for hydrogen (c) and electrolyte (d) transport computed based on (2.16a,b). Insets in (c,d) show a closer view of Sherwood variation for the highest current density in the statistically steady state. Current density at each case is distinguished using the colour map whose range is shown in the colour bar.

increases in time in contrast to the electrolyte concentration, which is depleted at the electrode. For the one-dimensional pure-diffusion problem in the absence of the bubbles (diffusion in a semi-infinite medium with constant flux on the boundary) the analytical solution gives the time evolution of the cathodic concentrations, $\tilde{C}_{j,e}^*$, as (Bejan 1993)

$$\tilde{C}_{j,e}^*(t) - C_{j,0} = 2J_j \sqrt{\frac{t}{\pi D_j}}, \quad (3.1)$$

which has been provided for comparison at each current density in figures 3(a) and 3(b). Small differences between this solution and the simulation results are related to the presence of the adhering bubble on the electrode and the inactive area underneath it, which alters the local concentrations slightly. Major deviations from the analytical solution occur after the departure of the first bubble, which leads to significantly enhanced mixing. As a result, fresh electrolyte is transported to the electrode, replacing the gas-enriched and electrolyte-depleted solution there. Eventually, the system reaches an equilibrium in which the reaction and transport rates are balanced, such that the cycle-averaged concentrations remain constant in time.

A comparison of the behaviour for different current densities i is best done using the transient Sherwood numbers (2.16a,b) plotted in figures 3(c) and 3(d) for H_2 and H_2SO_4 , respectively. Prior to the first bubble departure from the electrode surface, time-dependent Sherwood numbers collapse to a single curve regardless of the current density, as do

those pertaining to the analytical solution of the pure diffusion problem. The bifurcation from the main trend happens after the detachment of the first bubble, i.e. transition to the convection, which takes place earlier at higher current density due to the higher oversaturation of the dissolved gas in the electrode boundary layer and faster bubble growth. Once the system is at equilibrium and the bubble generation rate no longer changes, the Sherwood numbers also approach an equilibrium value. Small oscillations around this value occur within each bubble cycle (see insets for the highest current density). For these, the minima of $\tilde{Sh}_{j,e}$ correspond to the detachment times after which the Sherwood numbers immediately increase and the maxima are the instants when the bubble lifetime starts, followed by a slow decrease during the growth time. Furthermore, due to the higher frequency of bubble generation and hence stronger mixing in the electrolyte, the effective mass-transfer rate at the electrode, reflected in the values of $\tilde{Sh}_{j,e}$ in equilibrium, is significantly enhanced at higher current densities.

In order to provide insight into the flow structure and scalar distribution in the equilibrium state, figure 4 displays snapshots of the hydrogen supersaturation, $\zeta_{\text{H}_2} = C_{\text{H}_2}/C_{\text{H}_2,\text{sat}} - 1$, overlaid with velocity vectors at different stages of the bubble evolution and for varying current densities. For the case with $|i| = 10^3 \text{ A m}^{-2}$, corresponding plots for the electrolyte concentration distribution are provided in figure 5. At this current density, a maximum electrolyte depletion of $\approx 15\%$ occurs at the electrode and, even in the most extreme case with $|i| = 10^4 \text{ A m}^{-2}$, this value does not exceed $\approx 70\%$, meaning that the electrolyte concentration remains finite in all cases even though the diffusion-limited current density, $|i|_{\text{diff}} = n_e F D_s C_{s,0}/L_z = 59.7 \text{ A m}^{-2}$, is exceeded significantly. The associated transport enhancement is due to a large-scale convective pattern that is established during the rise stage, with an up-draught stream in bubble column, downwelling flow along the (periodic) sidewalls and wall-parallel flow close to the electrode. At low current density (figure 4a), the bubble driving is highly intermittent as the convective motion dissipates during the long growth period. However, as the latter becomes shorter for larger i (figures 4(b) and 4(c)), the flow becomes more and more continuous and a strong circulation is visible throughout the entire bubble cycle at $|i| = 10^4 \text{ A m}^{-2}$ in figure 4(d). The convective pattern counteracts the penetration of the electrode boundary layer into the bulk by advecting the fresh electrolyte towards the electrode. This effect is stronger at higher currents due to the higher frequency of bubble formation driving a stronger flow. This can be also appreciated from figures 6(a) and 6(b), which compare the vertical profiles of normalised H_2 and H_2SO_4 at a location half-way between adjacent bubbles, where an appreciable drop in the electrode boundary layer thickness with increasing current density is observed, consistent with an enhanced mass transport.

3.1. Current dependence of the Sherwood number and bubble size effect

Next, we consider the current dependence of the Sherwood numbers of hydrogen and electrolyte transport, averaged over an entire bubble lifetime in the statistically steady state, which are plotted in figure 7(a,b), respectively. Apart from the case with $d_b = 0.5 \text{ mm}$ considered so far, these panels also include results for other bubble departure diameters. The trend of increasing Sh_j with increasing i , which was already evident in figure 3(c,d) for $d_b = 0.5 \text{ mm}$, is consistently observed for all these cases. The current dependence approximates a power-law scaling of $Sh_j \sim i^{1/3}$, especially for larger bubbles, but deviations occur for smaller bubbles at high current densities, where Sh_j increases significantly slower. It is further interesting to examine how $Sh_{\text{H}_2,e}$ and $Sh_{s,e}$ relate to each other, which we do by plotting the ratio $Sh_{s,e}/Sh_{\text{H}_2,e}$ in figure 7(c). Given that

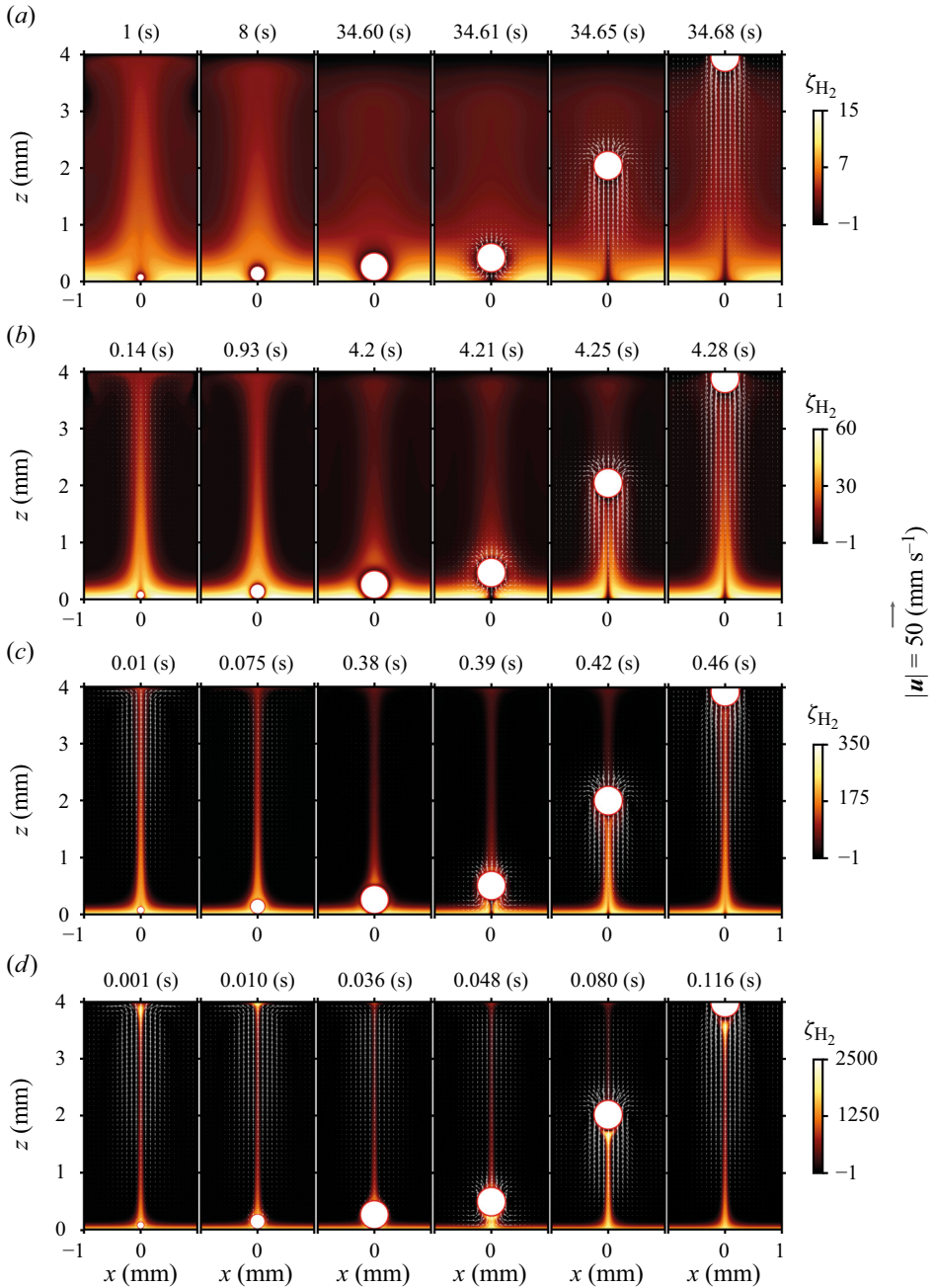


Figure 4. Snapshots of the hydrogen and velocity distributions in the equilibrium state at different stages of the bubble lifetime for current densities of (a) 10^1 , (b) 10^2 , (c) 10^3 and (d) 10^4 $A\ m^{-2}$. Bubble break-off diameter is $d_b = 0.5$ mm and spacing is set at $S = 2$ mm. In all cases, the first three images cover the bubble growth and the last three the bubble rise time. The supersaturation level, ζ_{H_2} , is shown using the colour bar. The superimposed vectors represent the induced velocity field by the growth and rise of the bubbles in the electrolyte. The velocity scale provided at the right of the figure applies to all panels.

Mass transport at gas-evolving electrodes

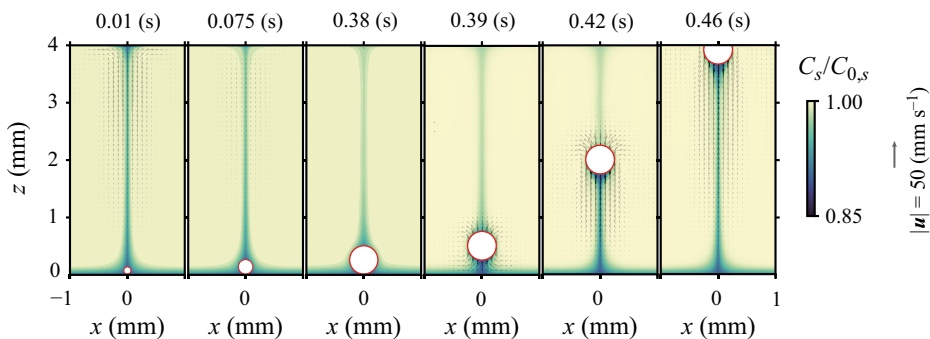


Figure 5. Snapshots of the electrolyte distribution for the case ($|i| = 10^3 \text{ A m}^{-2}$) shown in figure 4(c).

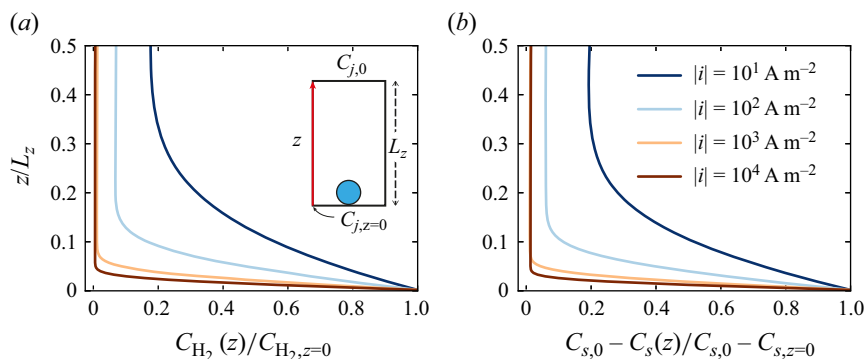


Figure 6. Vertical profiles of normalised hydrogen (a) and electrolyte (b) concentration half-way between adjacent bubbles (see the sketch in (a)) at the instant of bubble break-off. The profiles are captured at the statistically steady state for different current densities.

$Sh_{s,e}/Sh_{H_2,e} = \delta_{H_2}/\delta_s$, one expects this ratio to yield a constant of either $(D_{H_2}/D_s)^{1/2}$ (for diffusive transport) or $(D_{H_2}/D_s)^{1/3}$ (for convection given that the Schmidt number $Sc_j = D_j/\nu$ is large (Bejan 1993)) for a single-phase flow. In the present simulations, $D_{H_2}/D_s = 1.5$, such that the resulting values (1.22 and 1.14) do not differ significantly. In our results in figure 7(c), a ratio of comparable magnitude is attained for the smallest bubbles and similar values are also approached for the cases with larger d_b at successively larger magnitudes of i . The deviation from the single-phase value is related to the fact that the electrolyte is only transported in solution while hydrogen is also carried inside the bubble. It is therefore most pronounced at low current densities and for large bubble sizes since, for these cases, the fraction of gas transported in the bubbles is largest as the plot of f_G in figure 8(a) confirms. The gas efficiency decreases significantly with decreasing bubble size, but is only a weak function of the current density, especially for $i \lesssim 10^3 \text{ A m}^{-2}$. From the gas-evolution efficiency relation (2.18), it is deduced that $\tau_g \sim V_b(f_G i)^{-1}$, considering a constant rise time (τ_c) for bubbles with the same size. Given the weak dependence of f_G on i , the scaling of $\tau_g/V_b \sim i^{-1}$ holds reasonably well for all the cases shown here, as can be seen from figure 8(b).

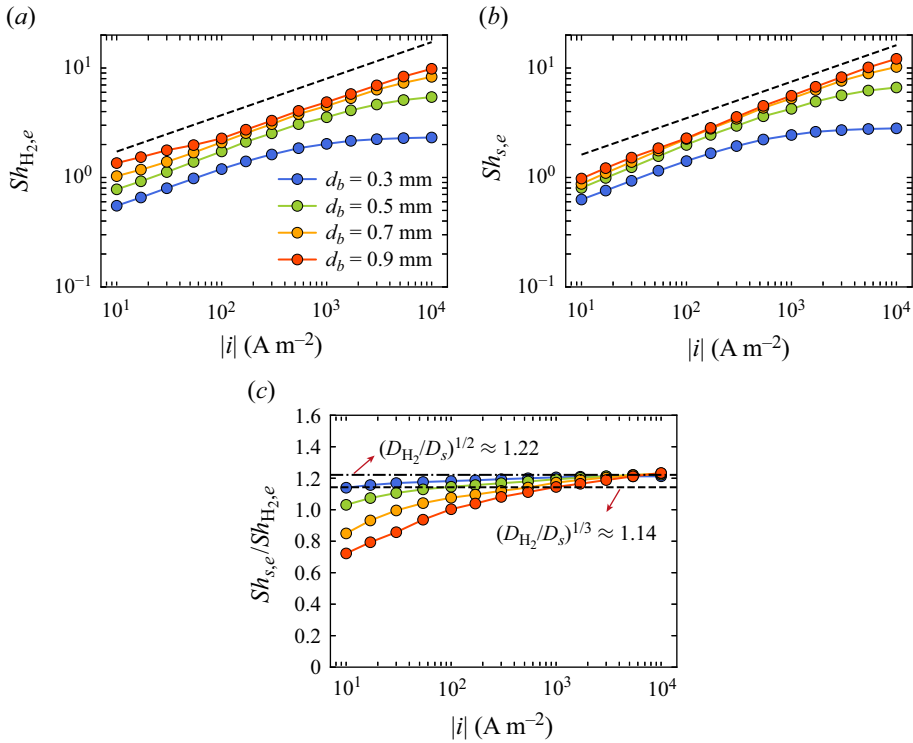


Figure 7. Sherwood number of (a) hydrogen and (b) electrolyte transport averaged over an entire bubble lifetime in the statistically steady state, as a function of current density for different bubble break-off diameters, d_b . The broken lines indicate the power-law relation $Sh_j \sim i^{1/3}$ for reference. (c) Ratio of electrolyte to hydrogen Sherwood numbers vs the current density at different bubble diameters. Dashed and dashed-dotted lines correspond to $(D_{H_2}/D_s)^{1/3}$ and $(D_{H_2}/D_s)^{1/2}$, respectively, for comparison.

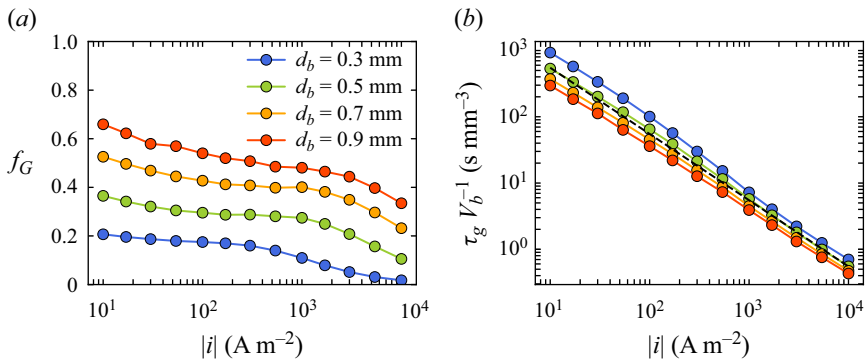


Figure 8. (a) Gas-evolution efficiency, f_G , as a function of current density for different bubble break-off diameters, d_b . (b) Bubble residence time, τ_g , compensated with bubble departure volume, V_b , as a function of current density for different values of d_b . The broken line indicates the power law of $\tau_g \sim i^{-1}$.

3.2. Effect of bubble spacing

Changing the bubble departure size, as was done in § 3.1, has multiple effects since it affects bubble growth times and the flow, but also alters the effective bubble coverage Θ . To disentangle these, we now fix the departure diameter of the bubble at $d_b = 0.5$ mm and

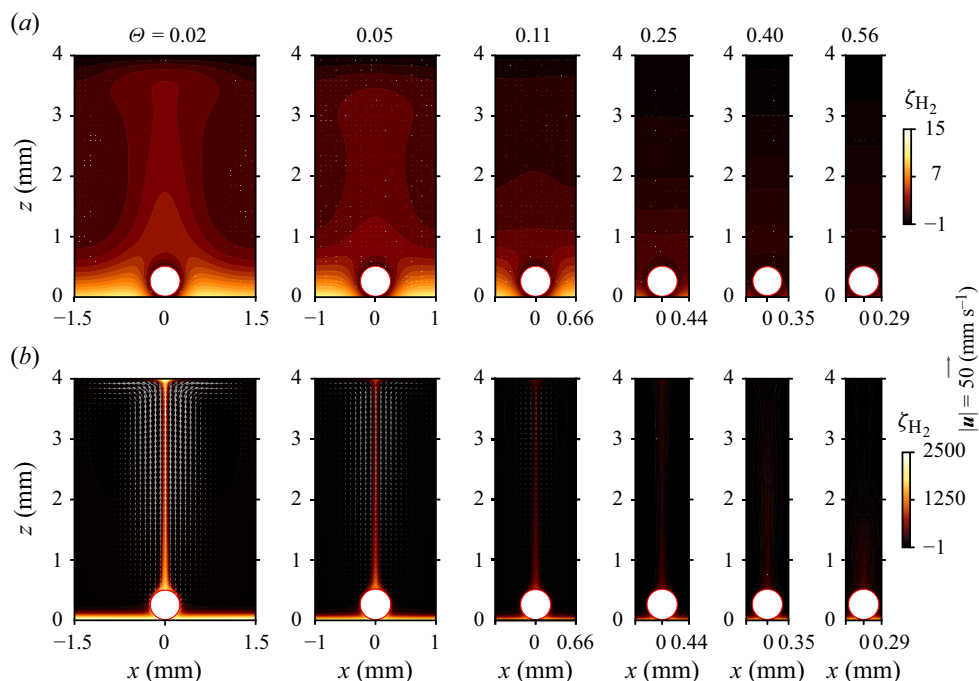


Figure 9. Snapshots of hydrogen supersaturation taken at the time of bubble detachment in the statistically steady state for $|i| = 10^1$ (a) and $|i| = 10^4$ A m^{-2} (b). The fractional bubble coverage is increased from left to right within the range $0.02 \leq \Theta \leq 0.56$ whose value is specified at top. The velocity scale applies to all panels.

vary the box size S to explore a range of $0.02 \leq \Theta \leq 0.56$. This resembles a change in the bubble population density, which in practice is tied to the current density and typically increases when i is increased (Vogt & Balzer 2005; Vogt 2013). Taking advantage of the numerical simulations, we can explore the effect of this parameter independently here.

Figures 9 and 10 offer insight into how changing Θ affects the mass-transport processes at the electrode by showing snapshots of the distributions of H_2 and H_2SO_4 , respectively, taken in the instant of bubble detachment after the system has reached a steady state. Figure 9(a) displays data for H_2 at the lowest current density investigated ($|i| = 10^1$ A m^{-2}). For this case, the boundary layers are thick due to the weak convective transport at low Θ . However, as the bubble coverage is increased, the amount of dissolved hydrogen decreases and almost all the produced gas is contained in the bubble at $\Theta = 0.56$. This implies very efficient transport for H_2 via the gas phase, but since the detachment frequency is low, the same does not hold for H_2SO_4 , as can be seen from figure 10(a). Here, the depletion boundary layer is very thick, with almost a linear gradient across the domain height. At the highest current density of $|i| = 10^4$ A m^{-2} , the significantly shorter detachment period leads to a much stronger driving of the flow. Convective transport therefore prevails even at high Θ , where τ_c tends to increase as the amount of hydrogen produced per bubble decreases for smaller bubble spacings (see figure 12c). As a consequence, not only the hydrogen boundary layer (figure 9b) but also that for the electrolyte concentration (figure 10) remains thin, even at $\Theta = 0.56$.

The trends observed in figures 9 and 10 are also reflected in the Sherwood numbers of H_2 and H_2SO_4 plotted in figures 11(a) and 11(b). Here, $Sh_{\text{H}_2,e}$ increases with Θ throughout the whole range of current densities investigated. Again, the data generally approximate

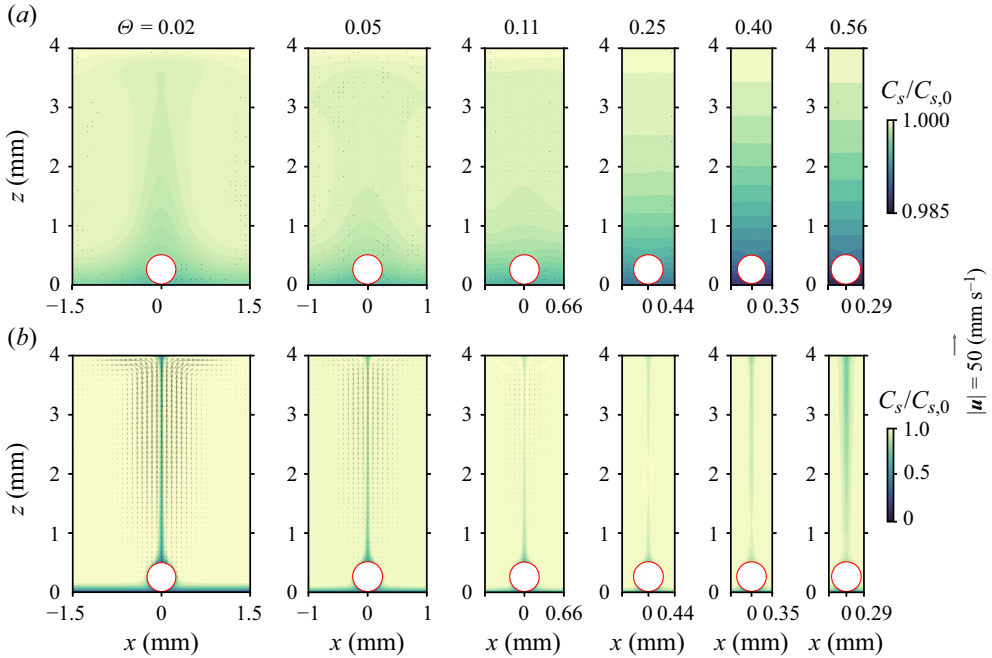


Figure 10. Snapshots of normalised H_2SO_4 distribution at the time of bubble detachment in the statistically steady state for $|i| = 10^1$ (a) and 10^4 A m^{-2} (b).

an $i^{1/3}$ scaling, albeit with significant deviations at low i and high Θ , where the results significantly exceed this trend. Additionally, $Sh_{\text{H}_2,e}$ falls below the $1/3$ -scaling line for large current densities and low bubble coverage, which is in accordance with the trend observed in figure 7(a) for smaller d_b for which the value of Θ is also reduced. For these higher currents, $Sh_{s,e}$ behaves similar to $Sh_{\text{H}_2,e}$ and this is also reflected in the ratio $Sh_{s,e}/Sh_{\text{H}_2,e}$ (figure 11c) being close to those expected for single-phase transport. Interestingly, $Sh_{s,e}/Sh_{\text{H}_2,e}$ attains values even slightly larger than 1.22 for larger Θ . Presumably, this is caused by the lower H_2 concentration in the dissolved phase, which dominates the transport for these cases. Remarkably, the Θ trend of $Sh_{s,e}$ at current densities $|i| \gtrsim 10^3 \text{ A m}^{-2}$ is opposite to that observed for the hydrogen transport in this regime with $Sh_{s,e}$ decreasing for larger Θ . The ratio $Sh_{s,e}/Sh_{\text{H}_2,e}$ drops to values as low as 0.1 for the most extreme case, confirming that the gas is predominantly carried in bubbles whose rise triggers no significant convection as the detachment frequency is low.

Corresponding results for the gas-evolution efficiency, f_G , are presented in figure 12(a). As expected, f_G increases significantly with fractional bubble coverage, Θ . It approaches unity at lower currents and for the tightest spacings, consistent with the observations in figures 9(a) and 11(c). Furthermore, f_G generally decreases at higher current densities because the more frequent detachment events drive an increasingly stronger convection. As a result, the bulk of the gas is transported in dissolved form at $|i| = 10^4 \text{ A m}^{-2}$ even at the highest coverage of $\Theta = 0.56$. When comparing our data with the empirical relation provided by Vogt (2011b), it is important to keep in mind that, in practice, increasing current density leads to higher Θ . To identify realistic combinations of i and Θ in the simulations, we compare the parameter space with the $\Theta(i)$ -relation given by Vogt & Balzer (2005) in figure 12(c). Simulations lying close to this line are marked with filled symbols in figure 12(a–c). When considering these data points only, our results for

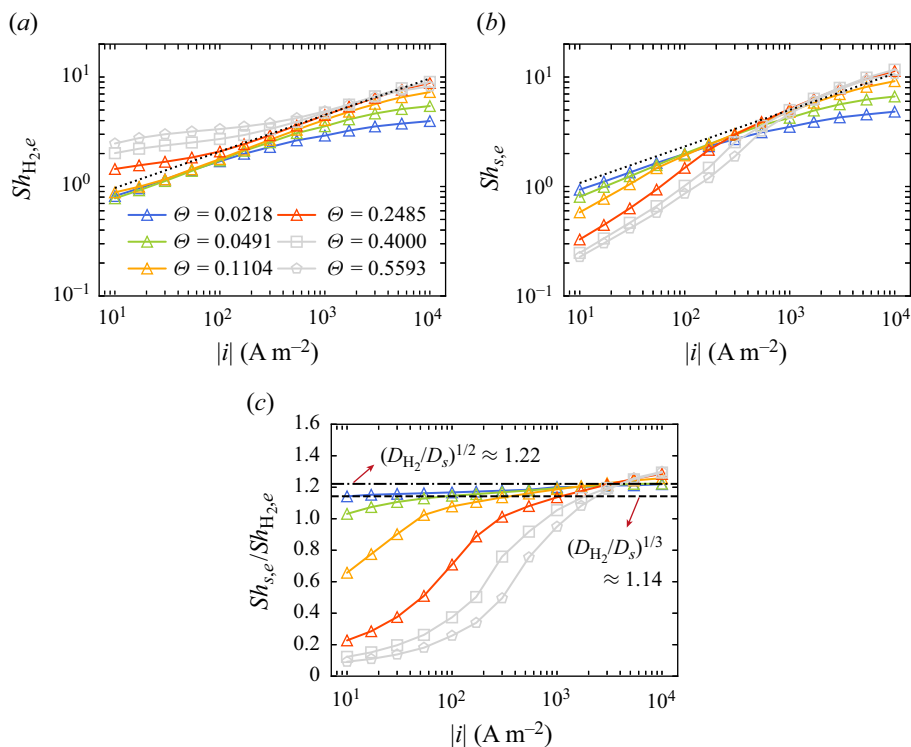


Figure 11. Sherwood number of (a) hydrogen and (b) electrolyte transport averaged over one bubble lifetime in the statistically steady state, as a function of current density for different bubble spacings. The bubble departure diameter is fixed at $d_b = 0.5$ mm and the range of fractional bubble coverage is $0.02 \leq \Theta \leq 0.56$, as specified in the legend.

f_G in figure 12(a) approximately agree with the empirical relation for $|i| \sim 10^3$ $A\ m^{-2}$, but differences arise for higher and in particular for low current densities $|i| \leq 10^2$ $A\ m^{-2}$.

The results for f_G are replotted in figure 12(b), but this time as a function of Θ since this is the practically more relevant form. It also allows for a comparison with the relations provided by Vogt (2011b, 2013), Vogt & Stephan (2015) and Vogt (2017) based on theoretical considerations (see dashed grey and green lines in figure 9b). An obvious difference is that empirical relations are independent of i , whereas the data at any given Θ exhibit a significant variation depending on the current density. This difference is significantly less prominent when considering only the ‘realistic’ cases. This implies that the change in Θ approximately accounts for the dependence on i within this subset. Results for the ‘realistic’ parameter combinations are also reasonably well approximated by the expression of Vogt (2017), at least up to $\Theta \approx 0.3$.

Figure 12(c) also includes results for the hydrogen supersaturation on the electrode in the steady state, $\zeta_{H_2,e}$, which are shown as colour contours interpolated between the simulation data points. Remarkably, the ‘realistic’ cases close to the relation of Vogt & Balzer (2005) are seen to cover a very wide range of $\zeta_{H_2,e} \approx 10$ up to very high values exceeding 10^3 . It should be noted, however, that for the latter cases, the boundary layers are very thin (see figure 9b), such that the effective supersaturation on the scale of the bubble will be significantly lower.

As a final point, we plot the bubble lifetime, τ_c , in figure 12(d). To compensate for the $1/i$ -dependence, which leads to variations in τ_c over 4 orders of magnitude, the data are

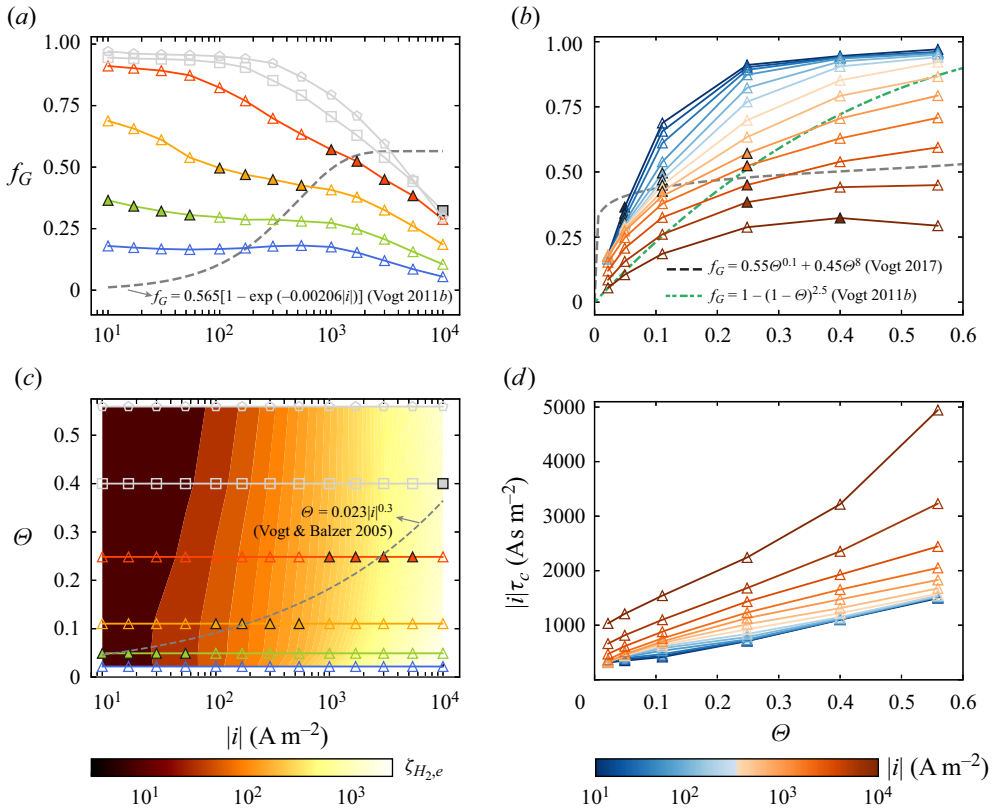


Figure 12. (a) Gas-evolution efficiency, f_G , as a function of current density for varying bubble spacings (specified in terms of the fractional bubble coverage, Θ). The bubble departure diameter has been fixed at $d_b = 0.5$ mm. (b) Gas-evolution efficiency vs bubble coverage for varying current densities. (c) Hydrogen supersaturation on the electrode surface, $\zeta_{H_2,e}$, for all the simulation cases with varying current density and bubble spacing. (d) Bubble lifetime, τ_c , premultiplied by current density as a function of bubble coverage for varying current densities. The relevant empirical relations by Vogt *et al.* are provided with broken lines in the panels. The filled markers in (a,b) show the closest data to the empirical relation $\Theta = 0.023|i|^{0.3}$ (Vogt & Balzer 2005) in (c), to highlight the more realistic cases.

premultiplied by i . For $f_G = \text{const.}$, all curves in the presented form would be expected to collapse onto a single line with linear dependence on Θ based on (2.18). While the linear trend is approximately preserved for all but the highest current density, the variations in f_G lead to an increase in $i\tau_c$ with i that is most pronounced for the highest current densities.

3.3. Relating the electrode mass transfer to the effective buoyancy driving

The goal of this section is to provide scaling relations for the mass transport at the electrode based on the relevant physical transport mechanism. Our results so far have already highlighted the relevance of the convective flow driven by the departing bubbles. There is an analogy between the present configuration and single-phase buoyancy-driven convection in the sense that the detaching bubbles resemble the plumes of buoyant liquid in the latter case (Climent & Magnaudet 1999). Analyses based on boundary-layer theory for convective heat transfer along vertical plates yield the power-law dependence on the Rayleigh number Ra^m , where the exponent m asymptotically varies from 1/4 for laminar flows to 1/3 for turbulent flows at high Ra (Churchill & Chu 1975). The same power laws

have empirically been shown to be valid for the convective heat transfer over horizontal plates and in particular for single-phase free-convective mass transfer over upward-facing horizontal electrodes by Wragg (1968). Beyond the laminar regime featuring an exponent of 0.25, these authors provided the relation

$$Sh = 0.16(GrSc)^{0.33}, \quad (3.2)$$

for the mass transport in the turbulent regime, where the Grashof number Gr captures the buoyancy forcing and the Schmidt number is given by $Sc = \nu/D$. For two-phase buoyancy-driven convection, Gr can be defined to account for the effective buoyancy provided by the bubbles according to

$$Gr = \frac{gd_b^3}{\nu^2} \frac{\rho_L - \rho_e}{\rho_e} = \frac{gd_b^3}{\nu^2} \frac{\rho_L - [(1 - \epsilon)\rho_L + \epsilon\rho_G]}{(1 - \epsilon)\rho_L + \epsilon\rho_G}, \quad (3.3)$$

where ρ_L is the density of the bulk electrolyte, ρ_e is the mixture density at the electrode surface, ρ_G is the gas density and ϵ is the gas volume fraction. Considering $\rho_G \ll \rho_L$ yields the simplified expression

$$Gr = \frac{gd_b^3}{\nu^2} \frac{\epsilon}{1 - \epsilon}. \quad (3.4)$$

Based on the fact that a single bubble is contained in a box with base area A_e and height $u_b\tau_c$, where u_b denotes the bubble rise velocity, the gas volume fraction ϵ can be related to the volumetric flow rate of the gas, $\dot{V}_G = V_b/\tau_c$, by (Zuber 1963)

$$\epsilon = \frac{\dot{V}_G}{A_e u_b}. \quad (3.5)$$

For all cases investigated here we find that $\epsilon \ll 1$. Assuming Stokes drag for the bubbles with a no-slip interface yields the terminal velocity

$$u_b = \frac{1}{18} \frac{gd_b^2}{\nu} \frac{\rho_L - \rho_G}{\rho_L}, \quad (3.6)$$

which, along with (2.18), leads to the final expression for Gr as

$$Gr = 18f_G d_b \frac{i}{n_e F} \frac{\mathcal{R}T_0}{P_0 \nu}. \quad (3.7)$$

The ratio of buoyancy to viscous forces therefore depends linearly on the input parameters d_b , f_G , and in particular on i . Consequently, the experimentally reported scaling of $Sh \sim i^{1/3}$ (Janssen & Hoogland 1973; Janssen 1978; Janssen & Barendrecht 1979; Whitney & Tobias 1988) is equivalent to $Sh \sim Gr^{1/3}$, provided that the product of the other two parameters (d_b and f_G) in (3.7) ($d_b f_G$) remains approximately constant with i .

Next, we consider the dependence of the Sherwood numbers for the mass transport at the electrode on Gr . Figure 13(a) presents a plot of $Sh_{H_2,e}$ vs Gr for all data presented in §§ 3.1 and 3.2. In this form, the results very convincingly collapse onto a single line, indicating the power law of $Sh_{H_2,e} \sim Gr^{1/3}$, which supports the adoption of the single-phase concept in the present configuration. Remarkably, the ‘turbulent’ scaling exponent of 1/3 applies to the full range of Gr studied here, even though the flow is relatively weak and only

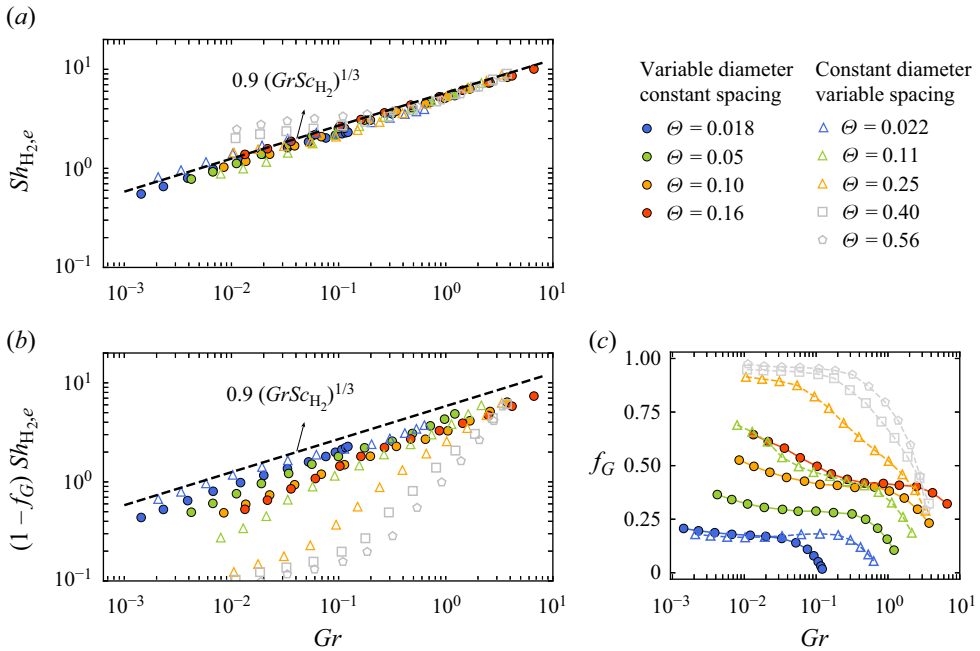


Figure 13. (a) Sherwood number of hydrogen transport, $Sh_{H_2,e}$ (2.16a,b), averaged over one bubble lifetime in the statistically steady state, vs Gr for all cases studied in this work. (b) Fractional Sherwood number of hydrogen transport as dissolved gas in the liquid phase, $(1 - f_G)Sh_{H_2,e}$. (c) Corresponding values of f_G vs Gr .

intermittent in some cases (see figures 4 and 9). The data in figure 13(a) are well described by the fit

$$Sh_{H_2,e} = 0.9(GrSc_{H_2})^{1/3}, \tag{3.8}$$

where the difference in the prefactor compared with the single-phase equivalent (3.2) is related to the multiphase nature of the present flow but also to the fact that a different length scale of bubble diameter is used here instead of the lateral length scale of the electrode by Wragg (1968). The only significant deviation from (3.8) occurs for the ‘slow’ (in terms of τ_c) cases featuring a high f_G , for which the gas transport (carried almost exclusively inside the bubbles) is more efficient than buoyancy driving would suggest.

It is important to note that, here, $Sh_{H_2,e}$ and therefore (3.8) accounts for the transport of both gaseous and dissolved hydrogen. We can focus on the dissolved transport specifically by multiplying $Sh_{H_2,e}$ with $(1 - f_G)$, as is done in figure 13(b). For reference, a plot of f_G for all data vs Gr is also included in figure 13(c). Consistent with the fact that there is a wide spread in f_G at any given Gr , there is no collapse of the data in figure 13(b), underlining that the analogy between single and multiphase buoyancy-driven flows is applicable at the level of the total transport only.

The transport of the electrolyte, which entirely acts as a passive scalar here, for the most part falls in line with the trends discussed for $Sh_{H_2,e}$. In particular, $Sh_{s,e}$ primarily follows the power law of $Sh_{s,e} \sim Gr^{1/3}$ even with the same prefactor when accounting for the difference in Sc , as shown in figure 14(a). However, in accordance with figures 7(c) and 11(c), $Sh_{s,e}$ drops below this scaling at low Gr and high θ . This means that electrolyte transport from the bulk to the electrode surface is limited when the bubbles highly cover the electrode surface and adhere to it for a long period during their lifetime.

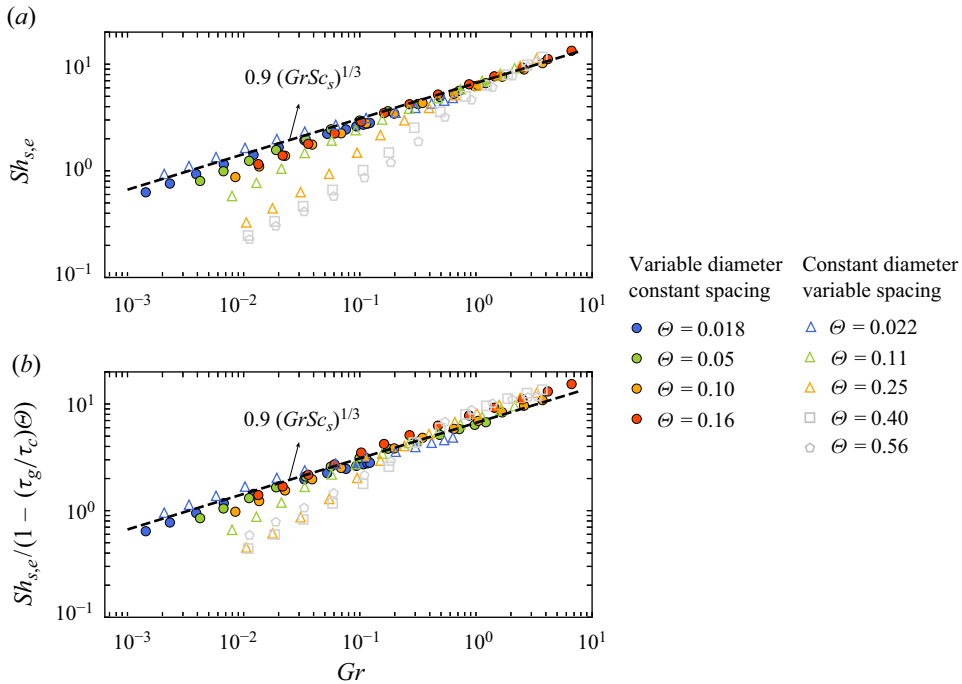


Figure 14. (a) Sherwood number of electrolyte transport, $Sh_{s,e}$ (2.16a,b), averaged over one bubble lifetime in the statistically steady state, vs Gr (3.3) for all cases studied in this work. (b) Value of $Sh_{s,e}$ compensated for net blockage effect, $\Theta\tau_g/\tau_c$, caused by bubbles adhering to the electrode surface in the residence time. The legend specifies cases simulated for different bubble diameters and spacings using the corresponding fractional bubble coverage of the electrode, Θ . The broken lines indicate the fitted power law, $Sh_{s,e} = 1.0(GrSc_s)^{1/3}$, in which $Sc_s = \nu/D_s$.

According to Vogt (1989, 2012), a factor contributing to the lower transport of the electrolyte is the blockage effect due to the presence of the bubble, as can be seen from the snapshots in figure 10(a). To account for this, we divide $Sh_{s,e}$ by the factor $(1 - \Theta\tau_g/\tau_c)$ in figure 14(b). Here, $1 - \Theta$ is the fraction of the electrode not covered by the bubble and the additional time scale ratio accounts for the fact that the blockage applies only during the growth time τ_g . Introducing this correction in fact reduces the deviations at lower Gr somewhat (but not fully) and the effect may therefore be relevant in this regime. However, the data for $Gr \gg 1$ are overcompensated. In summary, it therefore appears that the fact that no sustained convection exists at high bubble coverages if Gr is low plays the most important role leading to the lower electrolyte transport. This leads to limitation in the applicability of the single-phase analogy for this case. Nevertheless, it is worth noticing that the agreement with the 1/3 scaling law is much better for $Sh_{s,e}$ (figure 14a) than for dissolved H_2 (figure 13b), even though transport is exclusively within the electrolyte in both cases.

4. Mass transfer to the bubble

4.1. Bubble growth regimes

We now consider the dynamics of bubble growth and mass transfer into the bubble in more detail. The growth of the electrolytically generated gas bubbles can be approximated by an

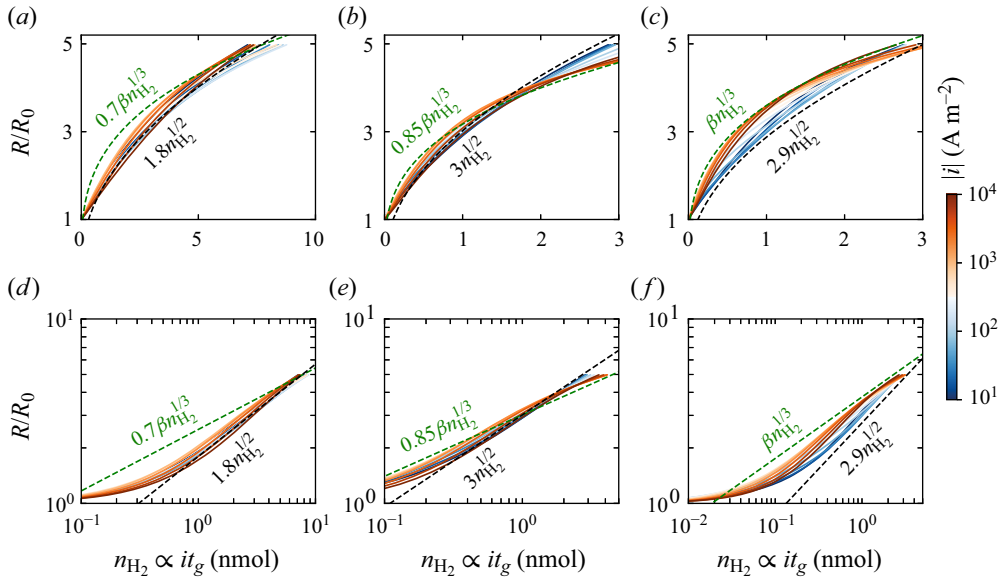


Figure 15. Temporal evolution of normalised bubble radius, R/R_0 , vs the molar amount of hydrogen produced in the cathodic reaction, $n_{\text{H}_2} = J_{\text{H}_2} A_e t_g$, where t_g is the time elapsed from the start of the bubble life in the stationary steady state. The results are for all the investigated current densities (distinguished with the colour map) at bubble coverages of $\Theta = 0.05$ (a) $\Theta = 0.25$, (b) and $\Theta = 0.40$ (c). The second row (d,e) shows the same data as in (a–c) but with logarithmic scaling. The green and black broken lines show the power laws with exponents of $1/3$ and $1/2$, respectively. The prefactors for the $1/3$ power law are adjusted relative to the growth constant of purely reaction-limited bubble growth, $\beta = 3.6 \text{ nmol}^{-1/3}$.

effective power law of

$$R(t) = \mathcal{B}t^x. \tag{4.1}$$

The limiting cases are as follows: during the very initial stage, when the growth of the bubble is strongly influenced by the inertia forces from the liquid (Slooten 1984), an exponent of $x = 1$ has been reported (Westerheide & Westwater 1961; Glas & Westwater 1964; Brandon & Kelsall 1985; Bashkatov *et al.* 2022). For later times, depending on whether the bubble growth is limited by the diffusive mass transfer of dissolved gas to the interface (Epstein & Plesset 1950; Scriven 1959; Westerheide & Westwater 1961) or by the gas production rate in the reaction (Darby & Haque 1973; Verhaart, de Jonge & van Stralen 1980; Yang *et al.* 2015; Bashkatov *et al.* 2022; Higuera 2022), exponents of $x = 1/2$ or $x = 1/3$ have been identified, respectively. However, in general, the effective value of the exponent in (4.1) deviates from these values due to the interplay between inertia, diffusion and reaction rates.

Figure 15 presents different growth dynamics in the statistically steady state, depending on current density and bubble coverage. Plotting the bubble radius vs the number of hydrogen moles, n_{H_2} , produced in the reaction from the beginning of the bubble’s lifetime, t_g , allows for easy comparison of the bubble growth dynamics over time for the full range of the current density. It is worth noting that $n_{\text{H}_2} = J_{\text{H}_2} A_e t_g$ and therefore $n_{\text{H}_2} \sim t_g$. Power laws with exponent $1/3$ and $1/2$ have been added for comparison in figure 15 at different bubble coverages. Here, corrections are fitted to the prefactor $\beta = (3\mathcal{R}T_0/4\pi R_0^3 P_0)^{1/3}$, which represents the value for purely reaction-limited growth (i.e. $f_G = 1$). For the lowest bubble coverage in figure 15(a), the growth dynamics is best described by the exponent

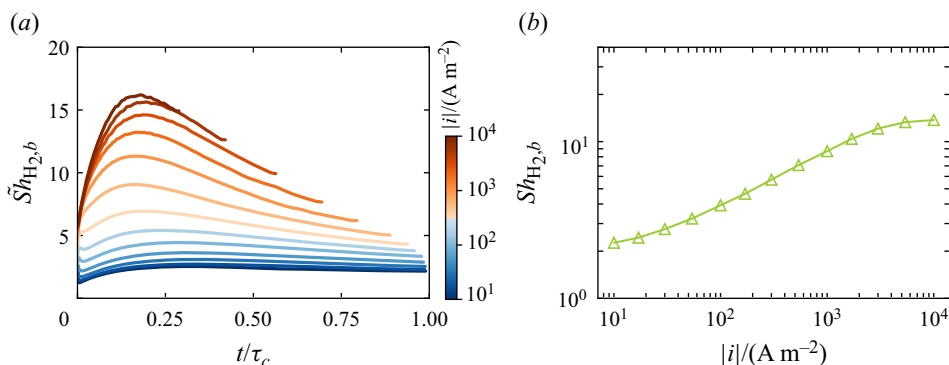


Figure 16. (a) Temporal evolution of the Sherwood number for the bubble, $\tilde{Sh}_{H_2,b}$ (2.17), during the entire bubble lifetime, τ_c , in the statistically steady state and across the entire range of current density distinguished using the colour map. The data correspond to the case with bubble departure diameter of $d_b = 0.5$ mm and a bubble spacing of $S = 2$ mm, which leads to bubble coverage of $\Theta = 0.1104$. (b) The corresponding averaged (over the bubble residence time τ_g) Sherwood number of the bubble, $Sh_{H_2,b}$, over the residence time, τ_g , plotted against the current density.

of $x = 1/2$ at all current densities. This indicates that the rate of mass transfer to the bubble is controlled by the diffusive transfer of dissolved hydrogen to the bubble interface for these cases. However, a switch from $x = 1/2$ to $1/3$ is appreciable as the current density increases at higher bubble coverages of $\Theta = 0.25$ and 0.40 , as presented in figures 15(b) and 15(c). At first sight, it may seem counter-intuitive that the reaction rate becomes more relevant as a limiting factor when it is increased. However, as discussed in the previous section, an increase in current density also significantly intensifies the convective transport, which is then predominantly in the dissolved phase even at high Θ . This reduces the boundary-layer thickness and the amount of dissolved H_2 (see figures 4 and 9), such that diffusive transport becomes increasingly less relevant compared with the faster reaction rate. Therefore, the exponent approaches $x = 1/3$ and the prefactor approaches β , as observable from figures 15(b) and 15(c) where the bubble size evolution is better described by such power law at higher bubble coverages and current densities.

4.2. Quantification of mass transport to the bubble

Figure 16(a) shows the transient behaviour of $Sh_{H_2,b}$ according to (2.17) over one bubble lifetime in the statistically steady state for varying current densities. Since bubble growth is neglected during the rise stage (see § 2.2.2 for further details), $Sh_{H_2,b}$ becomes equal to zero after the bubble break-off from the electrode surface. In figure 16(a), it can be observed that, at low current densities, an equilibrated mass-transfer rate to the bubble is established towards the end of the bubble residence time. This is evident from nearly constant values of $Sh_{H_2,b}$ at late stages of the growth phase, for current densities $|i| < 10^3 A m^{-2}$. In contrast, at higher current densities, $Sh_{H_2,b}$ remains in a transient all the way until the departure of the bubble. To study the mass transport to the bubble, the instantaneous $\tilde{Sh}_{H_2,b}$ is averaged over the bubble residence time, τ_g . The corresponding results for the data presented in figure 16(a) are shown in figure 16(b) and indicate an increase of $Sh_{H_2,b}$ with increasing current density.

To gain a broader understanding of hydrogen transport to the bubble and facilitate its quantification, we have plotted $Sh_{H_2,b}$ against current density in figure 17(a) for all the

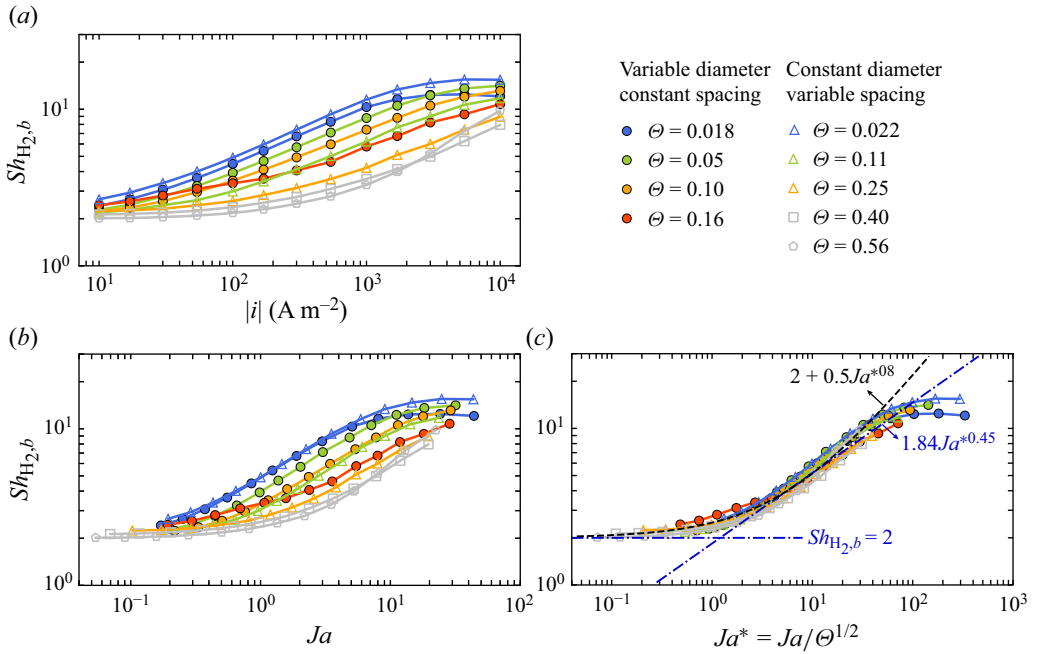


Figure 17. (a) Sherwood number of hydrogen transport to the bubble, $Sh_{H_2,b}$, averaged over the bubble residence time, τ_g , in the statistically steady state, as a function of the current density for all the simulation cases with varying bubble size or spacing. (b) Value of $Sh_{H_2,b}$ vs Jakob number, Ja , computed according to (4.2). (c) Value of $Sh_{H_2,b}$ vs Ja^* , i.e. the Jakob number corrected with $\Theta^{0.5} \approx d_b/S$ to account for the interference of the mass-transfer boundary layers on the bubbles with each other. An approximate fit to the data and the two asymptotes are shown with black and blue broken lines, respectively. The legend specifies cases simulated for different bubble diameters, d_b , and spacings, S , using the corresponding fractional bubble coverage of the electrode, Θ .

simulation cases, including those with variable bubble size or spacing. It is evident that, at low current densities, $Sh_{H_2,b}$ is nearly constant and then it starts to ramp up with current density for all of the simulated cases. Furthermore, the lower values of $Sh_{H_2,b}$ at higher Θ suggests that the normalised mass transfer to the bubble tends to decrease with bubble coverage.

The current density is not directly related to the mass transfer into the bubble. In fact, the driving force for bubble growth is the concentration difference across the boundary layer developing at the bubble interface. The latter can be normalised with the gas concentration inside the bubble to yield the Jakob number, Ja (Verhaart *et al.* 1980; Vogt 1984a, 2011a):

$$Ja = \frac{M_G}{\rho_G} \Delta C = \frac{\mathcal{R}T_0}{P_0} (C_{H_2,e} - C_{H_2,sat}), \quad (4.2)$$

where M_G is the hydrogen molar mass and $C_{H_2,e}$ is employed to estimate the concentration difference ΔC across the bubble boundary layer. At low $Ja \ll 1$, radial convection is negligible, such that $Sh_{H_2,b}$ remains constant. At moderate ($Ja \approx 1$) values and beyond, theoretical considerations suggest that the bubble Sherwood number becomes dependent only on Ja , and no other parameter (Epstein & Plesset 1950; Scriven 1959; Verhaart *et al.* 1980; Vogt 2011a). However, the plot of $Sh_{H_2,b}$ vs Ja for our results in figure 17(b) fails to collapse all the data onto a single curve. The reason for this is that in the theoretical considerations the effect of spatial confinement is not taken into account and

the bubble is assumed to be in an infinitely large medium. However, especially for large Θ , the growing bubbles interact and thereby enhance the effect of radial convection. This interaction becomes more prominent the smaller the bubble spacing S is relative to the bubble diameter d_b . It therefore seems useful to define a compensated Jakob number $Ja^* = Ja/\Theta^{1/2}$ which additionally depends on the ratio $\Theta^{1/2} \approx d_b/S$. Figure 17(c) reports the results of $Sh_{H_2,b}$ vs the compensated Jakob number Ja^* . Now a reasonable collapse of the data is achieved. An approximated fitting to the data gives

$$Sh_{H_2,b} = 2 + 0.5Ja^{*0.8}. \tag{4.3}$$

It is shown as a black broken line in figure 17(c). It is worth noting that, for very low values of bubble coverage, particularly at $\Theta = 0.018$ and $\Theta = 0.022$, once again a nearly constant $Sh_{H_2,b}$ can be observed towards the upper limit of Ja^* (as shown in figure 17(c)) where deviation from (4.3) occurs. This is related to the very short residence time of the bubble at very high current densities for these cases. As seen in the transient behaviour of $Sh_{H_2,b}(t)$ in figure 16(a), as the current density increases, the bubble departs from the electrode at increasingly earlier times before an equilibrated mass transfer to the bubble can be established. This leads to nearly constant averaged $Sh_{H_2,b}$ for such cases in figure 17(c), where a deviation from (4.3) occurs.

The relation (4.3) for the mass transfer to the bubble is consistent with the classical theories of Epstein & Plesset (1950) and Scriven (1959) for bubble growth in an infinitely large and uniformly supersaturated solution. The problem was later modified by Verhaart *et al.* (1980) to account for bubble growth over electrodes with non-uniform supersaturation around the bubble. The theories show a constant bubble Sherwood number of $Sh_{H_2,b} = 2$ for small values of Jakob number, $Ja \rightarrow 0$. Such a condition is maintained in our simulations for high bubble coverages and low current densities where the concentration variation within the boundary layer is relatively low. The functional form used to represent the increase of $Sh_{H_2,b}$ for larger Ja^* in (4.3) follows that suggested by Vogt (2011a), as an approximation of the exact solution of Verhaart *et al.* (1980).

It is useful to reformulate the definition of the Jakob number in terms of the Péclet number of mass transfer at the electrode, Pe^* (defined as the ratio of reaction to diffusion rates), and $Sh_{H_2,e}$, as

$$Ja^* = \frac{Pe^*}{\Theta^{1/2}Sh_{H_2,e}}, \quad \text{with } Pe^* = \frac{i}{2F} \frac{\mathcal{R}T_0}{P_0} \frac{d_b}{D_{H_2}}. \tag{4.4}$$

Substituting the empirical fit (3.8) for $Sh_{H_2,e}$, together with (4.3), leads to

$$Sh_{H_2,b} = 2 + 0.5 \left[\frac{Pe^*}{\Theta^{1/2}0.9(GrSc_{H_2})^{1/3}} \right]^{0.8}. \tag{4.5}$$

The Grashof number can be expressed as $Gr = 18f_GPe^*/Sc_{H_2}$ (see (3.7)) such that the final mass-transfer relation for the bubble is given by

$$Sh_{H_2,b} = 2 + 0.28 \left(\frac{Pe^{*2/3}}{\Theta^{1/2}f_G^{1/3}} \right)^{0.8}. \tag{4.6}$$

Since Pe^* and Θ only depend on input parameters, the only previously unknown variable in (4.6), just as in (3.8), is the gas-evolution efficiency f_G . In order to enable a prediction solely based on input parameters, in the next section we will establish a suitable relation for f_G .

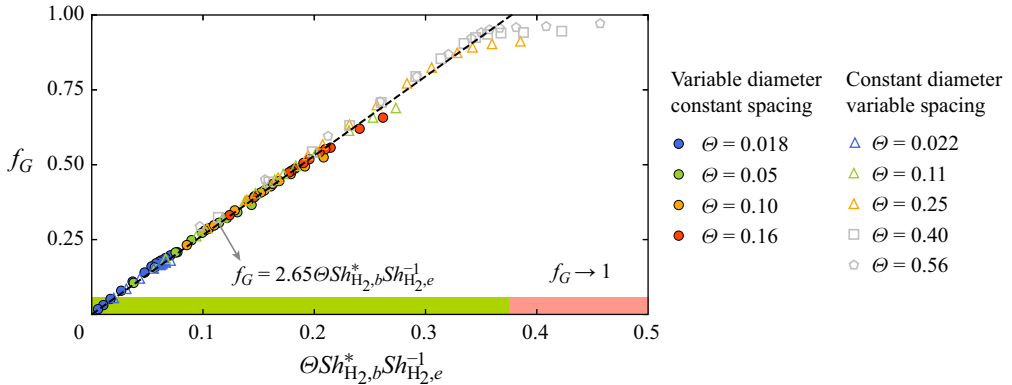


Figure 18. Gas-evolution efficiency, f_G , vs the dimensionless group $\Theta Sh_{H_2,b}^* Sh_{H_2,e}^{-1}$. The broken line shows the linear fit with slope $\alpha = 2.65$ for $\Theta Sh_{H_2,b}^* Sh_{H_2,e}^{-1} < 0.375$, highlighted with green. For $\Theta Sh_{H_2,b}^* Sh_{H_2,e}^{-1} > 0.375$, highlighted with red, the gas-evolution efficiency approaches its upper bound, $f_G \rightarrow 1$.

5. Gas-evolution efficiency

In steady-state conditions, we can restate the definition of the gas-evolution efficiency f_G in (2.18) in terms of the cycle-averaged molar fluxes into the bubble and at the electrode according to

$$f_G = \frac{\int_0^{\tau_c} \int_{\partial V} D_{H_2} \nabla C_{H_2} \cdot \hat{n}_b \, dA_b \, dt}{\int_0^{\tau_c} \int_{A_e} D_{H_2} \nabla C_{H_2} \cdot \hat{n}_e \, dA_e \, dt} \sim \frac{D_{H_2} \frac{(C_{H_2,e} - C_{H_2,sat})}{\delta_b} d_b^2}{D_{H_2} \frac{(C_{H_2,e} - C_{H_2,0})}{\delta_e} A_e}, \quad (5.1)$$

where δ_b and δ_e are the boundary-layer thicknesses normal to the bubble interface and electrode surface, respectively. Using $Sh_{H_2,b}^* \sim d_b/\delta_b$, $Sh_{H_2,e} \sim d_b/\delta_e$, $\Theta \sim d_b^2/A_e$ and noting that $(C_{H_2,e} - C_{H_2,sat})/(C_{H_2,e} - C_{H_2,0}) \approx 1$, this leads to the expression

$$f_G = \alpha \Theta \frac{Sh_{H_2,b}^*}{Sh_{H_2,e}}, \quad (5.2)$$

where the prefactor α is to be determined from the data. The difference between $Sh_{H_2,b}$ and $Sh_{H_2,b}^*$ is that the former is averaged over the bubble residence time, τ_g , whereas the latter is averaged over the entire bubble lifetime, τ_c , consistent with the definition of f_G (2.18). Since bubble growth is disregarded during rise stage, $Sh_{H_2,b}(t) = 0$ during this period such that the different definitions of the Sherwood numbers are related by $Sh_{H_2,b}^* = (\tau_g/\tau_c) Sh_{H_2,b}$.

Next, in figure 18 the gas-evolution efficiency f_G for all of the cases simulated here is plotted as a function of the dimensionless group, $\Theta Sh_{H_2,b}^* Sh_{H_2,e}^{-1}$. All data collapse onto a single line for $\Theta Sh_{H_2,b}^* Sh_{H_2,e}^{-1} < 0.375$, consistent with (5.2). The slope is obtained as $\alpha = 2.65$ based on the linear fit indicated as a dashed line in the figure. For $\Theta Sh_{H_2,b}^* Sh_{H_2,e}^{-1} > 0.375$, the gas-evolution efficiency approaches its upper limit $f_G \rightarrow 1$ and the data level off close to this value.

Inserting $Sh_{H_2,e}$ from (3.8) and $Sh_{H_2,b}$ from (4.6) into (5.2) results in an implicit expression for f_G that cannot be solved explicitly (see Appendix B). Instead, we resort

to piecewise solutions for f_G by inserting the asymptotes of $Sh_{H_2,b}$ indicated by dashed blue lines in [figure 17\(c\)](#), into (5.2). Doing so yields the explicit expressions

$$f_G = 1.835\Theta^{3/4}Pe^{*-1/4}, \quad \text{for } Ja^* \lesssim 1, \quad (5.3)$$

$$f_G = 1.257\Theta^{0.522}Pe^{*-0.0225}, \quad \text{for } Ja^* \gtrsim 1. \quad (5.4)$$

It should be noted that, in the derivation of (5.3) and (5.4), we have taken $Sh_{H_2,b} = Sh_{H_2,b}^*$ presuming that $\tau_g/\tau_c \approx 1$, i.e. the bubble rise time is negligible. This is valid for our simulations at low and moderate current densities, whereas at high current densities, τ_g ultimately becomes even smaller than the bubble rise time, τ_r , violating this assumption (e.g. see [figure 4d](#)). This can be considered an artefact of the simulations in which there is always a single bubble inside the computational box and the next bubble is initialised once the previous one has left the domain from the top boundary. Therefore the wait time is equal to the bubble rise time, τ_r , whereas experiments have revealed that the wait time is extremely short, especially at high current densities where the supersaturation level adjacent to the nucleation spot is very high (Jones, Evans & Galvin 1999; Brussieux *et al.* 2011; Yang *et al.* 2015). Therefore, the wait time is insignificant and it can be safely considered that $Sh_{H_2,b}^* = Sh_{H_2,b}$ for practical applications.

For reference, in [Appendix B](#) we have included explicit relations for $Sh_{H_2,e}$ and $Sh_{H_2,b}$, resulting from combining (5.3) and (5.4) with (3.8) and (4.6).

6. Further discussions and conclusions

In this work, we set out to identify and quantify the governing mass-transfer mechanism at gas-evolving electrodes by means of direct numerical simulations. Our work provides details on the mass-transfer processes on a horizontal electrode subjected to successive growth and rise of electrolytically generated gas bubbles. We employed the IBM to enforce the mass and momentum interfacial conditions on the bubble surface and, therefore, to solve for its growth rate as well as translational motion, employing Fick's law and particle equations of motion, respectively. To elucidate the main effects, we varied the current density within the range of $10 \leq |i| \leq 10^4 \text{ A m}^{-2}$ for different prescribed bubble sizes and spacings, expressed as fractional bubble coverage Θ of the electrode surface.

We quantified the cumulative hydrogen transport from the electrode surface (as dissolved gas and within the gas bubble) in [figure 13](#) and that of electrolyte transport to the electrode in [figure 14](#). By drawing an analogy to single-phase heat- and mass-transfer problems, the buoyancy-driven convection induced by consecutively departing bubbles from the electrode surface was identified as the governing mass-transfer mechanism. This finding was corroborated by a unique power law of $Sh_{j,e} = 0.9(GrSc_j)^{1/3}$, which was found to describe the hydrogen transport, and to a large part also the electrolyte transport at the electrode. For the electrolyte, a factor of $(1 - \Theta)$ to compensate for the surface blockage effect reduces, yet does not fully eliminate, deviations from the power law at low Gr . No such deviations occur at high Gr , at which also most of the gas transport is in the dissolved state.

It is interesting to note that the observed 1/3-scaling implies that the dimensional mass flux is independent of the length scale used in defining Sh and Gr . Other definitions, such as utilising the height of the domain as in Climent & Magnaudet (1999) or Lakkaraju *et al.* (2013), are therefore just as valid. Nevertheless, the choice of d_b is preferred here for consistency with earlier studies and practicality. Drawing on the corresponding heat-transfer regime in Rayleigh–Bénard convection (see e.g. Malkus 1954; Grossmann &

Lohse 2000), the physical interpretation of this finding is that the mass transport is determined by the laminar boundary layers. The convective transport in the bulk, on the other hand, is so efficient that its details (such as the domain height) do not influence the overall rate. Reassuringly, this also implies independence of the domain height in our simulations, as is indeed observed (see Appendix C).

Furthermore, we found a connection between the bubble growth dynamics and the hydrogen transport rate from the electrode. Specifically, as Gr increases with increasing current density and bubble coverage of the electrode, the growth dynamics of the bubble switches from a diffusion-controlled, $R = \alpha t^{1/2}$, to a reaction-controlled, $R = \beta t^{1/3}$, regime (see figure 15). This transition can be attributed to the high transport rate of hydrogen from the electrode surface at large Gr which prevailed over the gas production rate, thereby limiting the available oversaturation that would favour diffusive growth. Next, we quantified the hydrogen transport to the bubble as a function of the Jakob number Ja . Our data showed no collapse when plotted against the conventional definition of Ja . The agreement was much better when additionally incorporating the ratio $d_b/S \sim \Theta^{1/2}$ into the definition of a modified Jakob number, Ja^* , to account for the effect of neighbouring bubbles. With this modified definition, the resulting expression for mass transfer into the bubble is given by (4.6).

Finally, we established a semi-empirical relation between the dimensionless mass-transfer rates at the electrode and bubble interface and the gas-evolution efficiency f_G . Ultimately, this allowed us to provide explicit (i.e. depending on input parameters only) expressions for f_G given by (5.3) and (5.4) and consequently also for the other response parameters $Sh_{H_2,e}$ and $Sh_{H_2,b}$ (see Appendix B). These findings can help quantify mass-transfer rates in practical applications, provided typical bubble sizes and spacings on the electrode can be quantified.

Our findings reveal a different governing physics of mass transfer at gas-evolving electrodes than was envisioned by Stephan & Vogt (1979), Vogt (2011b) and Vogt & Stephan (2015), who attributed the rate-controlling mechanism of mass transfer to micro-processes induced by bubble growth and break-off from the electrode. As briefly introduced in § 1, these micro-processes originate from three different sources: pure diffusion of fresh electrolyte to the electrode surface in the small region previously occupied by the bubble, convective flow induced by the expanding boundary of the bubble and wake flow after its break-off from the electrode. These processes impact the mass transfer in a microarea surrounding the nucleation spot whose size declines in time due to the bubble growth. For pure-diffusion transport of the reactant to the electrode during bubble growth, Vogt & Stephan (2015) modified the mass-transfer relations established by Roušar & Cezner (1975). To account for microconvection of bubble growth and break-off, they considered an analogy of the flow pattern around a growing bubble to lateral plug flow (Stephan & Vogt 1979), which was later modified with a boundary-layer flow (Vogt & Stephan 2015). This approach allowed them to employ the mass-transfer relations developed for such flows over a flat plate to quantify the averaged transport of reagent to the microarea within the time interval of bubble growth and break-off. They concluded that micro-processes in the small region surrounding the bubble were the rate-determining mechanism of mass transfer and prevailed over single-phase and two-phase free convection at moderate and high values of current density (Vogt 2011b).

Our results are inconsistent with these considerations due to several reasons. Vogt & Stephan (2015) assumed that the space previously occupied by the bubble was fully replenished with fresh electrolyte immediately after bubble break-off, and hence they employed Cottrell's relationship to predict the pure-diffusion mass transfer at

the microarea. While this assumption holds true to some extent for high current densities, it is violated at low currents where the electrode boundary layer is much larger than the bubble break-off diameter (the bubble is fully immersed in the boundary layer, see [figure 4](#)). In such cases, stirring the solution in a region that is already depleted of reactant fails to fully replace the bubble volume with fresh bulk electrolyte. Likewise, the employed analogy to plug/boundary-layer flow over a flat plate is questionable because the predominantly wall-parallel advection of a depleted boundary layer caused by bubble growth hardly affects the wall-normal mass transfer. Consequently, we fail to observe enhanced mixing during growth periods in our simulations.

In contrast, our findings provide evidence that the flow pattern established by two-phase buoyancy-driven convection (see [figure 4](#)) is key in setting the mass-transfer rate at the electrode. It is clearly visible from the H_2 and H_2SO_4 concentration snapshots in [figures 4](#) and [5](#) that the concentration fields are changed in accordance with the flow pattern induced by bubble motion; i.e. an up-draught in the bubble column, descent of the solution mixture between the bubbles and a roughly wall-parallel flow adjacent to the electrodes. Such a flow pattern is analogous to those induced by plume emissions in single-phase free convection. In fact, the similarity of the mass-transfer relations established in this work ([3.8](#)) to those of single-phase free convection (Wragg [1968](#); Churchill & Chu [1975](#)) proves that two-phase buoyancy-driven convection of departing bubbles is the rate-controlling mechanism of mass transfer at gas-evolving electrodes. This is further consistent with experimental measurements by Janssen & Hoogland ([1973](#)), Janssen ([1978](#)) and Janssen & Barendrecht ([1979](#)) where the thickness of the boundary layer on hydrogen-evolving electrodes followed the same power law as ([3.8](#)) when the bubble coalescence did not happen frequently. In summary, it therefore does not appear necessary to account for micro-processes, such as bubble growth, specifically when considering mass transfer.

There remain some limitations that apply to this work. To avoid additional complications, we only allowed a single bubble in the domain at any given time. This is a limitation at the highest current densities considered here, where the rise time, and hence the waiting time before the nucleation of a new bubble, dominates the overall cycle. Furthermore, we did not take into account the potential contribution of single-phase free convection, which arises from density gradients in the solution caused by concentration variations in the electrode and bubble boundary layers (Ngamchuea *et al.* [2015](#); Novev & Compton [2018](#)). Single-phase free convection might be of some influence at low current densities, where the bubbles adhere to the electrode for a long period of time and allow the density gradients in the electrode boundary layer to develop to a sufficient extent necessary for triggering the instabilities (Sepahi *et al.* [2022](#)). However, Sepahi *et al.* ([2022](#)) found that these instabilities are suppressed for bubble spacings of less than ≈ 2 mm, which is the case for most of the simulation cases here except those with the least bubble coverage of the electrode. At higher values of the current density where the frequency of bubble generation is relatively high, the induced flow of departing bubbles is very likely to suppress the single-phase free convection by reducing the density gradients in the cell or prevailing over it if both mechanisms coexist.

Another neglected effect is the Marangoni convection (Sternling & Scriven [1959](#); Yang *et al.* [2018](#); Park *et al.* [2023](#)) arising from surface tension gradients along the interface due to the temperature increase or electrolyte depletion in the bubbles' proximity. Thermal Marangoni flow is mostly playing a role in electrolytically generated gas bubbles on microelectrodes where the current density can easily surpass 10^6 A m⁻² in the bubble foot area and increase the temperature remarkably by ohmic heating (Yang *et al.* [2018](#); Massing *et al.* [2019](#); Hossain *et al.* [2022](#); Bashkatov *et al.* [2023](#)). However, thermal Marangoni is

likely less of a factor in the present configuration, as our current density does not exceed 10^4 A m^{-2} , which is not sufficient to increase the temperature considerably. However, solutal Marangoni as a result of electrolyte depletion (Park *et al.* 2023) might play a role, which needs further investigation in future works. Finally, as our numerical solver treats the full three-dimensional problem, we are able to extend this work to a set-up in which several bubbles are generated in a asymmetrical network of nucleation spots to study the collective effects of bubbles and to replicate a system which mimics the relevant physics more accurately for practical applications.

Supplementary material. All data supporting this study are openly available from the 4TU. Research Data repository at <https://doi.org/10.4121/9d6fe69a-c5ea-4e0e-ae96-302b59f68d69>

Acknowledgments. We thank Professor A. Prosperetti for fruitful discussions.

Funding. This work was supported by the Netherlands Center for Multiscale Catalytic Energy Conversion (MCEC), an NWO Gravitation programme funded by the Ministry of Education, Culture and Science of the government of the Netherlands. This project has received funding from the European Research Council (ERC) under the European Union’s Horizon 2020 research and innovation programme (grant agreement no. 950111, BU-PACT). This project has received funding from the European Union’s Horizon 2020 research and innovation programme under the Marie Skłodowska-Curie (grant agreement no. 801359). We acknowledge PRACE for awarding us access to MareNostrum at Barcelona Supercomputing Center (BSC), Spain, and Irene at Très Grand Centre de calcul du CEA (TGCC), France, under project no. 2021250115.

Declaration of interests. The authors report no conflict of interest.

Author ORCIDs.

- Farzan Sepahi <https://orcid.org/0000-0002-1581-2162>;
- Roberto Verzicco <https://orcid.org/0000-0002-2690-9998>;
- Detlef Lohse <https://orcid.org/0000-0003-4138-2255>;
- Dominik Krug <https://orcid.org/0000-0002-0627-5676>.

Appendix A. Code verification

A.1. Validation of bubble motion with IBM

A remedy is required to solve (2.12) for the bubble motion with IBM due to stability issues that arise at low gas to liquid density ratios. To mitigate this, the virtual mass approach by Schwarz *et al.* (2015) is employed here and a virtual force, $F_v = C_v \rho_L (du_b/dt)$, with C_v denoting a coefficient of order 1, is added to both sides of (3.6). Since F_v is evaluated explicitly on the right-hand side but implicitly on the left-hand side, this increases the diagonal dominance of the inversion coefficient in the case of very low gas–fluid density ratio $\Gamma = \rho_G/\rho_L \ll 1$. We resort to a virtual mass method with standard IBM here due to the rather simple wake flow of the light rising bubbles at low Reynolds number. In case of a higher Reynolds number, at which wake instabilities lead to complex flow motion, one may consider using more robust but computationally much more demanding methods like IBM with a strong coupling of fluid–structure interaction (Borazjani, Ge & Sotiropoulos 2008) or the IBM projection method (Lācis, Taira & Bagheri 2016; Assen *et al.* 2024). In this context, it is also worth noting that the surface integral relating to the hydrodynamic force on the bubble can be evaluated efficiently by relating it to the IBM forcing term, f_u , as follows (Uhlmann 2005; Breugem 2012; Kempe & Fröhlich 2012):

$$\int_{\partial V_b} \boldsymbol{\tau} \cdot \hat{\mathbf{n}}_b \, dA = -\rho_L \int_{V_b} \mathbf{f}_u \, dV + \rho_L \frac{d}{dt} \left(\int_{V_b} \mathbf{u} \, dV \right). \tag{A1}$$

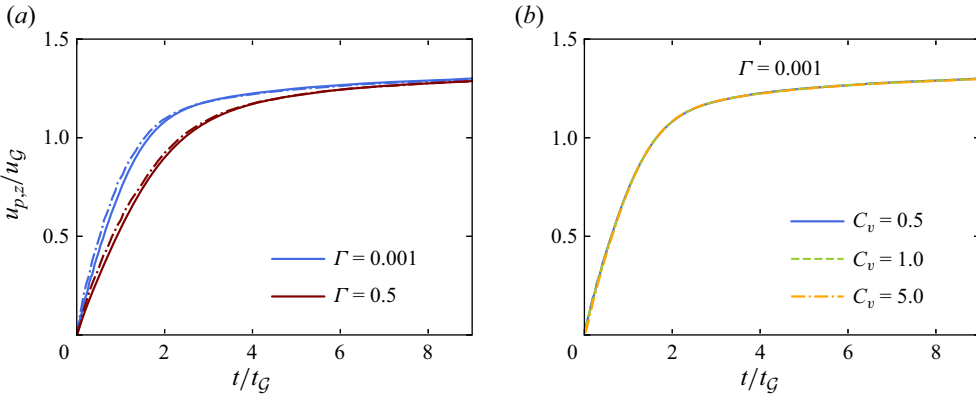


Figure 19. (a) Temporal evolution of the normalised particle rise velocity for Galilei number $Ga = 170$ at density ratios $\Gamma = 0.001$ and 0.5 , obtained from the present work (solid lines) and comparison with data from Schwarz, Kempe & Fröhlich (2015) (broken lines). Virtual mass coefficients of $C_v = 0.5$ and 0 have respectively been used for density ratios $\Gamma = 0.001$ and 0.5 . (b) Sensitivity of rise velocity to virtual mass coefficient for $\Gamma = 0.001$.

To check the reliability of our method, we simulate the test case of Schwarz *et al.* (2015) using our code. The ascending motion of a light particle with density ratios of $\Gamma = 0.5$ and 0.001 in a quiescent viscous fluid is considered. Such flows are characterised by the Galileo number defined as

$$Ga = \frac{\sqrt{|\Gamma - 1|gd_b^3}}{\nu}. \tag{A2}$$

Additionally, the gravitational velocity and time scales read

$$u_G = \sqrt{|\Gamma - 1|gd_b} \quad \text{and} \quad t_G = \sqrt{\frac{d_b}{|\Gamma - 1|g}}, \tag{A3a,b}$$

respectively, and are utilised as reference values. The related parameters considered here are $Ga = 170$, $g = \|\mathbf{g}\| = 10$, $d_b = 1$ and $\rho_L = 1$. The size of the computational box is set to $L = (6.4, 6.4, 12.8)d_b$ and is discretised with $N = (256, 256, 512)$ cells in the x, y and z directions, respectively. The sphere is initially at rest and released at $x_{b,0} = (3.2, 3.2, 0.6)d_b$. Periodic boundary conditions are applied in all directions and time marching is performed with steps of $\Delta t = 1 \times 10^{-3}$ to exactly replicate the test case in Schwarz *et al.* (2015). The simulation for $\Gamma = 0.5$ is stable without modification of the original equation and is therefore run with $C_v = 0$. Stability for $\Gamma = 0.001$ is ensured by setting $C_v = 0.5$. Figure 19(a) presents the results for the time evolution of the particle rise velocity u_p , along with the corresponding data from Schwarz *et al.* (2015), with which excellent agreement is observed. Furthermore, we have performed the simulations for $\Gamma = 0.001$ using different values of C_v to check the sensitivity of results to the artificial virtual force. Figure 19(b) shows that the particle rise velocity is quite insensitive to the virtual mass. Hence, we conclude that this method can safely be employed to simulate the rising motion of electrolytically generated gas bubbles with $\Gamma = 0.001$ in this work.

A.2. Grid-independence check

To ensure the accuracy of the simulations, a grid-independence check has been performed on the case presented in § 3 with $d_b = 0.5$ mm and $S = 2$ mm. The highest current density

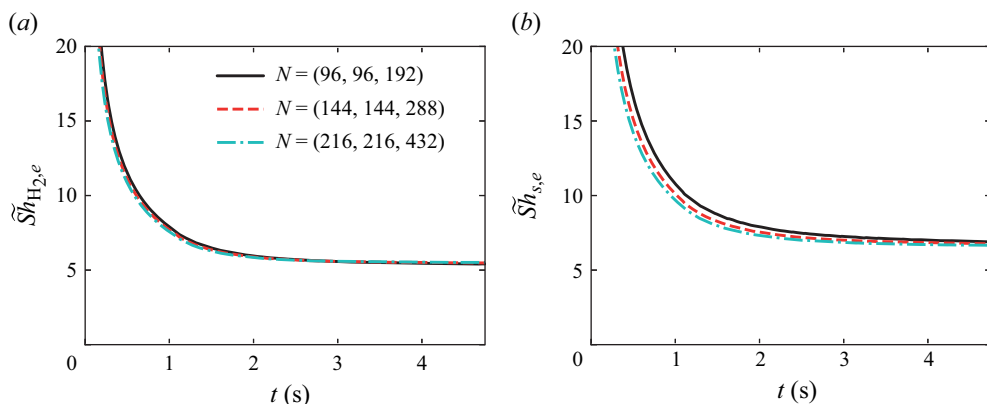


Figure 20. Grid-independence check based on the on temporal evolution of H₂ (a) and H₂SO₄ (b) Sherwood numbers on the electrode surface for the case presented in § 3, i.e. $d_b = 0.5$ mm and $S = 2$ mm at the highest current density of $|i| = 10^4$ A m⁻². Base-grid sizes, introduced in (a), are refined by factor of 2 for H₂ transport. Grid-independent results have been achieved for both species.

of $|i| = 10^4$ A m⁻² featuring the thinnest boundary layer on the electrode (cf. figure 4) is selected for this purpose. Figures 20(a) and 20(b) show the time evolution of the H₂ and H₂SO₄ Sherwood numbers on the electrode surface for three grids with increasing resolution, confirming that the results are independent of the grid size in the investigated range. The base grids are refined by a factor of two for H₂ using a multiple resolution strategy, as explained in § 2.2.1. This strategy ensures the hydrogen conservation in the system by sufficiently resolving the boundary-layer thickness on the bubble interface (see Appendix A.3). Grid refinement is only applied for H₂ transport, as dissolved hydrogen and its diffusion into the bubble determine the bubble dynamics and hence the whole hydrodynamics and mass transfer in the system. Based on the results in figure 20, the base-grid resolution of $N = (144, 144, 288)$ is selected for the reference case and grid sizes for other cases with varying lateral size of the computational box have been adjusted to keep the spatial resolution constant. This results in 36 grid cells across the bubble diameter if $d_b = 0.5$ mm, whereas this value is 21 if $d_b = 0.3$ mm.

A.3. Hydrogen conservation

Obviously, it is crucial to assure that the fluxes of dissolved hydrogen into the bubble interface, yielding the bubble growth rate, are accurately calculated with IBM, respecting mass conservation. To this end, we perform an analysis to check the conservation of hydrogen in the system. This requires that the rate of change of H₂ moles dissolved in the bulk electrolyte should be balanced with the net of H₂ interfacial fluxes. The latter include the H₂ production rate on the electrode surface ($J_{H_2,e}$), the desorption rate at the bubble interface ($J_{H_2,b}$) and the outflux at the top boundary ($J_{H_2,top}$). Figure 21 compares the net interfacial fluxes with the rate of change of H₂ in solution during bubble growth. This analysis concerns the reference case presented in § 3 ($d_b = 0.5$ mm and $S = 2$ mm) in the statistically steady state. It is evidenced by figure 21 that our numerical scheme is conservative for hydrogen gas within the studied range of current density. However, higher current densities most likely demand finer spatial and temporal resolutions in order to capture the extremely thin mass boundary layers developed on the bubble and electrode interfaces.

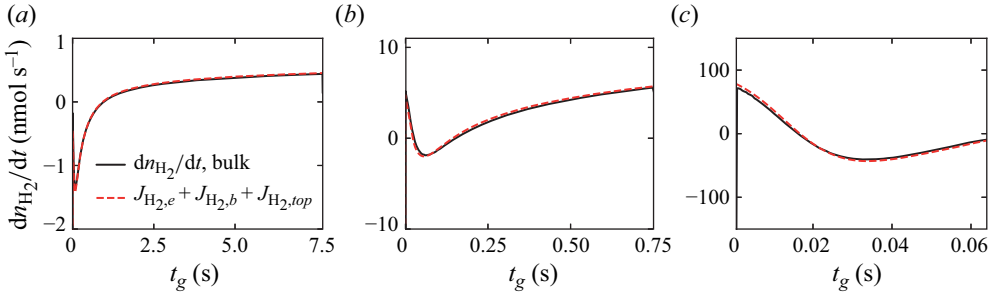


Figure 21. Hydrogen conservation check during the bubble residence time on the electrode at the statistically steady state, performed for the case presented in § 3, i.e. $d_b = 0.5$ mm and $S = 2$ mm at current densities $|i| = 54$ (a), 540 (b), 5400 A m⁻² (c). Here, t_g is the age of the bubble generated in the statistically steady state. Black solid lines are the rate of change of H₂ moles in the solution mixture. Red broken lines are the summation of H₂ production rate on the electrode ($J_{H_2,e}$), desorption rate into the bubble ($J_{H_2,b}$) and loss rate from the top boundary ($J_{H_2,top}$).

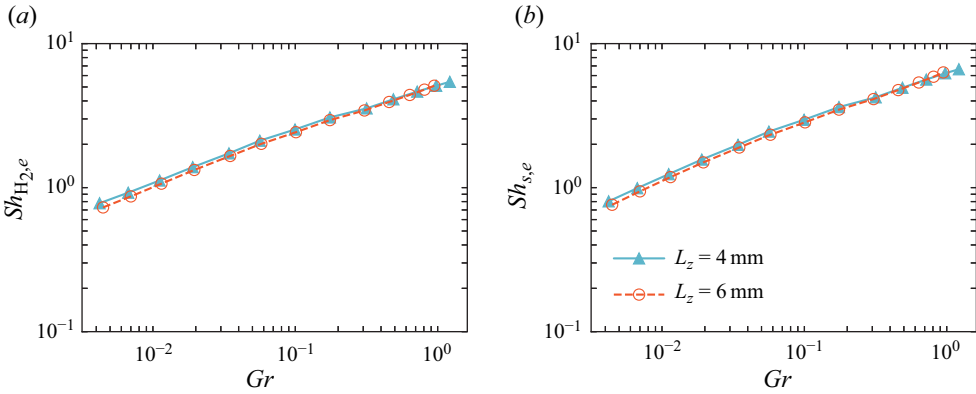


Figure 22. Sensitivity of the averaged Sherwood numbers of (a) hydrogen and (b) electrolyte transport at the electrode to the height of the computational domain. The test has been performed for the cases presented in § 3, i.e. $d_b = 0.5$ mm and $S = 2$ mm at different current densities.

Appendix B. Additional expressions

The implicit expression for the gas-evolution efficiency f_G , obtained by inserting (3.8) and (4.6) into (5.2), reads

$$f_G = 1.12\Theta \frac{2 + 0.28 \left(\frac{Pe^{*2/3}}{\Theta^{1/2} f_G^{1/3}} \right)^{0.8}}{(f_G Pe^*)^{1/3}}, \tag{B1}$$

which only has a piecewise solution. Inserting the expression for f_G given by (5.3) and (5.4) into the fit of $Sh_{H_2,e}$ given by (3.8) leads to an expression for $Sh_{H_2,e}$ solely based on input parameters as

$$Sh_{H_2,e} = 2.89(\Theta Pe^*)^{1/4}, \quad \text{for } Ja^* \lesssim 1, \tag{B2}$$

$$Sh_{H_2,e} = 2.55\Theta^{0.174} Pe^{*0.326}, \quad \text{for } Ja^* \gtrsim 1. \tag{B3}$$

Similarly, inserting (5.3) and (5.4) into (4.6) yields an expression for $Sh_{H_2,b}$ based on input parameters as

$$Sh_{H_2,b} = 2 + 0.238 \left(\frac{Pe^*}{\Theta} \right)^{0.6}, \quad \text{for } Ja^* \lesssim 1, \quad (B4)$$

$$Sh_{H_2,b} = 2 + 0.261 \left(\frac{Pe^*}{\Theta} \right)^{0.54}, \quad \text{for } Ja^* \gtrsim 1. \quad (B5)$$

Appendix C. Effect of domain height on electrode Sherwood numbers

To test how the results depend on the domain height, we have additionally run simulations for cases discussed in § 3 with an extended height $L_z = 6$ mm. As figure 22 shows, the effect is minimal.

REFERENCES

- ABDELOUAHED, L., HREIZ, R., PONCIN, S., VALENTIN, G. & LAPICQUE, F. 2014a Hydrodynamics of gas bubbles in the gap of lantern blade electrodes without forced flow of electrolyte: experiments and CFD modelling. *Chem. Engng Sci.* **111**, 255–265.
- ABDELOUAHED, L., VALENTIN, G., PONCIN, S. & LAPICQUE, F. 2014b Current density distribution and gas volume fraction in the gap of lantern blade electrodes. *Chem. Engng Res. Des.* **92** (3), 559–570.
- ANGULO, A., VAN DER LINDE, P., GARDENIERS, H., MODESTINO, M. & FERNÁNDEZ RIVAS, D. 2020 Influence of bubbles on the energy conversion efficiency of electrochemical reactors. *Joule* **4** (3), 555–579.
- ASSEN, M.P., WILL, J.B., NG, C., LOHSE, D., VERZICCO, R. & KRUG, D. 2024 Rising and settling 2-D cylinders with centre-of-mass offset. *J. Fluid Mech.* **981**, A7.
- BACZYMAŁSKI, D., KARNBACH, F., MUTSCHKE, G., YANG, X., ECKERT, K., UHLEMANN, M. & CIERPKA, C. 2017 Growth and detachment of single hydrogen bubbles in a magnetohydrodynamic shear flow. *Phys. Rev. Fluids* **2** (9), 1–19.
- BACZYMAŁSKI, D., KARNBACH, F., YANG, X., MUTSCHKE, G., UHLEMANN, M., ECKERT, K. & CIERPKA, C. 2016 On the electrolyte convection around a hydrogen bubble evolving at a microelectrode under the influence of a magnetic field. *J. Electrochem. Soc.* **163** (9), E248–E257.
- BASHKATOV, A., BABICH, A., HOSSAIN, S., YANG, X., MUTSCHKE, G. & ECKERT, K. 2023 H₂ bubble motion reversals during water electrolysis. *J. Fluid Mech.* **958**, A43.
- BASHKATOV, A., HOSSAIN, S.S., MUTSCHKE, G., YANG, X., ROX, H., WEIDINGER, I.M. & ECKERT, K. 2022 On the growth regimes of hydrogen bubbles at microelectrodes. *Phys. Chem. Chem. Phys.* **24** (43), 26738–26752.
- BASHKATOV, A., YANG, X., MUTSCHKE, G., FRITZSCHE, B., HOSSAIN, S.S. & ECKERT, K. 2021 Dynamics of single hydrogen bubbles at Pt microelectrodes in microgravity. *Phys. Chem. Chem. Phys.* **23** (20), 11818–11830.
- BATTISTELLA, A., AELEN, S., ROGHAI, I. & VAN SINT ANNALAND, M. 2018 Euler–Lagrange modeling of bubbles formation in supersaturated water. *Chem. Engng* **2** (3), 39.
- BEJAN, A. 1993 *Heat Transfer*. John Wiley & Sons.
- BOISSONNEAU, P. & BYRNE, P. 2000 An experimental investigation of bubble-induced free convection in a small electrochemical cell. *J. Appl. Electrochem.* **30** (7), 767–775.
- BORAZJANI, I., GE, L. & SOTIROPOULOS, F. 2008 Curvilinear immersed boundary method for simulating fluid structure interaction with complex 3D rigid bodies. *J. Comput. Phys.* **227** (16), 7587–7620.
- BRANDON, N.P. & KELSALL, G.H. 1985 Growth kinetics of bubbles electrogenerated at microelectrodes. *J. Appl. Electrochem.* **15** (4), 475–484.
- BREUGEM, W.-P. 2012 A second-order accurate immersed boundary method for fully resolved simulations of particle-laden flows. *J. Comput. Phys.* **231** (13), 4469–4498.
- BRUSSEUX, C., VIERS, P., ROUSTAN, H. & RAKIB, M. 2011 Controlled electrochemical gas bubble release from electrodes entirely and partially covered with hydrophobic materials. *Electrochim. Acta* **56** (20), 7194–7201.
- BURDYN, T., GRAHAM, P.J., PANG, Y., DINH, C.T., LIU, M., SARGENT, E.H. & SINTON, D. 2017 Nanomorphology-enhanced gas-evolution intensifies CO₂ reduction electrochemistry. *ACS Sust. Chem. Engng* **5** (5), 4031–4040.

- CARSLAW, H.S. & JAEGER, J.C. 1959 *Conduction of Heat in Solids*, 2nd edn. Oxford University Press.
- CHURCHILL, S.W. & CHU, H.H. 1975 Correlating equations for laminar and turbulent free convection from a vertical plate. *Intl J. Heat Mass Transfer* **18** (11), 1323–1329.
- CLIMENT, E. & MAGNAUDET, J. 1999 Large-scale simulations of bubble-induced convection in a liquid layer. *Phys. Rev. Lett.* **82** (24), 4827–4830.
- DARBAND, G.B., ALIOFKHAZRAEI, M. & SHANMUGAM, S. 2019 Recent advances in methods and technologies for enhancing bubble detachment during electrochemical water splitting. *Renew. Sust. Energy Rev.* **114** (February), 109300.
- DARBY, R. & HAQUE, M. 1973 The dynamics of electrolytic hydrogen bubble evolution. *Chem. Engng Sci.* **28** (5), 1129–1138.
- DAWOOD, F., ANDA, M. & SHAFIULLAH, G. 2020 Hydrogen production for energy: an overview. *Intl J. Hydrogen Energy* **45** (7), 3847–3869.
- DICKINSON, E.J.F., LIMON-PETERSEN, J.G. & COMPTON, R.G. 2011 The electroneutrality approximation in electrochemistry. *J. Solid State Electrochem.* **15** (7–8), 1335–1345.
- DUKOVIC, J. & TOBIAS, C.W. 1987 The influence of attached bubbles on potential drop and current distribution at gas-evolving electrodes. *J. Electrochem. Soc.* **134** (2), 331.
- EPSTEIN, P.S. & PLESSET, M.S. 1950 On the stability of gas bubbles in liquid-gas solutions. *J. Chem. Phys.* **18** (11), 1505–1509.
- FRITZ, W. 1935 Berechnung des maximalvolumens von dampfblasen. *Physik. Z.* **36**, 379–384.
- GLAS, J. & WESTWATER, J. 1964 Measurements of the growth of electrolytic bubbles. *Intl J. Heat Mass Transfer* **7** (12), 1427–1443.
- GROSSMANN, S. & LOHSE, D. 2000 Scaling in thermal convection: a unifying theory. *J. Fluid Mech.* **407**, 27–56.
- HIGUERA, F. 2021 A model of the growth of hydrogen bubbles in the electrolysis of water. *J. Fluid Mech.* **927**, A33.
- HIGUERA, F.J. 2022 Evolution of hydrogen bubbles at the surface of a porous horizontal cathode. *Phys. Rev. Fluids* **7** (11), 113602.
- HOLLADAY, J., HU, J., KING, D. & WANG, Y. 2009 An overview of hydrogen production technologies. *Catal. Today* **139** (4), 244–260.
- HOSSAIN, S.S., BASHKATOV, A., YANG, X., MUTSCHKE, G. & ECKERT, K. 2022 Force balance of hydrogen bubbles growing and oscillating on a microelectrode. *Phys. Rev. E* **106** (3), 035105.
- HREIZ, R., ABDELOUAHED, L., FÜNFSCILLING, D. & LAPICQUE, F. 2015a Electrogenerated bubbles induced convection in narrow vertical cells: a review. *Chem. Engng Res. Des.* **100**, 268–281.
- HREIZ, R., ABDELOUAHED, L., FÜNFSCILLING, D. & LAPICQUE, F. 2015b Electrogenerated bubbles induced convection in narrow vertical cells: PIV measurements and Euler–Lagrange CFD simulation. *Chem. Engng Sci.* **134**, 138–152.
- IBL, N., ADAM, E., VENCZEL, J. & SCHALCH, E. 1971 *Chem. Ing. Technik* **403**, 202–215.
- IIDA, T., MATSUSHIMA, H. & FUKUNAKA, Y. 2007 Water electrolysis under a magnetic field. *J. Electrochem. Soc.* **154** (8), E112.
- IWASAKI, A., KANEKO, H., ABE, Y. & KAMIMOTO, M. 1997 Investigation of electrochemical hydrogen evolution under microgravity condition. *Electrochim. Acta* **43** (5–6), 509–514.
- IWATA, R., ZHANG, L., LU, Z., GONG, S., DU, J. & WANG, E.N. 2022 How coalescing bubbles depart from a wall. *Langmuir* **38** (14), 4371–4377.
- JANSSEN, L. 1978 Mass transfer at gas evolving electrodes. *Electrochim. Acta* **23** (2), 81–86.
- JANSSEN, L. & BARENDRECHT, E. 1979 The effect of electrolytic gas evolution on mass transfer at electrodes. *Electrochim. Acta* **24** (6), 693–699.
- JANSSEN, L. & HOOGLAND, J. 1970 The effect of electrolytically evolved gas bubbles on the thickness of the diffusion layer. *Electrochim. Acta* **15** (6), 1013–1023.
- JANSSEN, L.J. & HOOGLAND, J.G. 1973 The effect of electrolytically evolved gas bubbles on the thickness of the diffusion layer-II. *Electrochim. Acta* **18** (8), 543–550.
- JONES, S., EVANS, G. & GALVIN, K. 1999 Bubble nucleation from gas cavities – a review. *Adv. Colloid Interface Sci.* **80** (1), 27–50.
- KEMPE, T. & FRÖHLICH, J. 2012 An improved immersed boundary method with direct forcing for the simulation of particle laden flows. *J. Comput. Phys.* **231** (9), 3663–3684.
- KHALIGHI, F., DEEN, N.G., TANG, Y. & VREMAN, A.W. 2023 Hydrogen bubble growth in alkaline water electrolysis: an immersed boundary simulation study. *Chem. Engng Sci.* **267**, 118280.
- KIM, J. & MOIN, P. 1985 Application of a fractional-step method to incompressible Navier–Stokes equations. *J. Comput. Phys.* **59** (2), 308–323.

- KOZA, J.A., MÜHLENHOFF, S., ŻABIŃSKI, P., NIKRITYUK, P.A., ECKERT, K., UHLEMANN, M., GEBERT, A., WEIER, T., SCHULTZ, L. & ODENBACH, S. 2011 Hydrogen evolution under the influence of a magnetic field. *Electrochim. Acta* **56** (6), 2665–2675.
- LĀČIS, U., TAIRA, K. & BAGHERI, S. 2016 A stable fluid–structure-interaction solver for low-density rigid bodies using the immersed boundary projection method. *J. Comput. Phys.* **305**, 300–318.
- LAKKARAJU, R., STEVENS, R.J.A.M., ORESTA, P., VERZICCO, R., LOHSE, D. & PROSPERETTI, A. 2013 Heat transport in bubbling turbulent convection. *Proc. Natl Acad. Sci. USA* **110** (23), 9237–9242.
- VAN DER LINDE, P., MORENO SOTO, Á., PEÑAS-LÓPEZ, P., RODRÍGUEZ-RODRÍGUEZ, J., LOHSE, D., GARDENIERS, H., VAN DER MEER, D. & FERNÁNDEZ RIVAS, D. 2017 Electrolysis-driven and pressure-controlled diffusive growth of successive bubbles on microstructured surfaces. *Langmuir* **33** (45), 12873–12886.
- LIU, G.R. & GU, Y.T. 2005 *An Introduction to Meshfree Methods and Their Programming*, 1st edn. Springer.
- LU, J., DAS, S., PETERS, E. & KUIPERS, J. 2018 Direct numerical simulation of fluid flow and mass transfer in dense fluid-particle systems with surface reactions. *Chem. Engng Sci.* **176**, 1–18.
- LUPO, G., GRUBER, A., BRANDT, L. & DUWIG, C. 2020 Direct numerical simulation of spray droplet evaporation in hot turbulent channel flow. *Intl J. Heat Mass Transfer* **160**, 120184.
- LUPO, G., NIAZI ARDEKANI, M., BRANDT, L. & DUWIG, C. 2019 An immersed boundary method for flows with evaporating droplets. *Intl J. Heat Mass Transfer* **143**, 118563.
- MALKUS, M.V.R. 1954 The heat transport and spectrum of thermal turbulence. *Proc. R. Soc. Lond. A* **225**, 196–212.
- MANDIN, P., DERHOUMI, Z., ROUSTAN, H. & ROLF, W. 2014 Bubble over-potential during two-phase alkaline water electrolysis. *Electrochim. Acta* **128**, 248–258.
- MANDIN, P., HAMBURGER, J., BESSOU, S. & PICARD, G. 2005 Modelling and calculation of the current density distribution evolution at vertical gas-evolving electrodes. *Electrochim. Acta* **51** (6), 1140–1156.
- MASSING, J., MUTSCHKE, G., BACZYMAŁSKI, D., HOSSAIN, S.S., YANG, X., ECKERT, K. & CIERPKA, C. 2019 Thermocapillary convection during hydrogen evolution at microelectrodes. *Electrochim. Acta* **297**, 929–940.
- MATSUSHIMA, H., IIDA, T. & FUKUNAKA, Y. 2013 Gas bubble evolution on transparent electrode during water electrolysis in a magnetic field. *Electrochim. Acta* **100**, 261–264.
- MATSUSHIMA, H., KIUCHI, D., FUKUNAKA, Y. & KURIBAYASHI, K. 2009 Single bubble growth during water electrolysis under microgravity. *Electrochem. Commun.* **11** (8), 1721–1723.
- MATSUSHIMA, H., NISHIDA, T., KONISHI, Y., FUKUNAKA, Y., ITO, Y. & KURIBAYASHI, K. 2003 Water electrolysis under microgravity. *Electrochim. Acta* **48** (28), 4119–4125.
- MORRIS, M.D. & LINGANE, J.J. 1963 The effect of electrical migration on the chronopotentiometric transition time. *J. Electroanal. Chem.* **6** (4), 300–313.
- NGAMCHUEA, K., ELOUL, S., TSCHULIK, K. & COMPTON, R.G. 2015 Advancing from rules of thumb: quantifying the effects of small density changes in mass transport to electrodes. Understanding natural convection. *Anal. Chem.* **87** (14), 7226–7234.
- NIKOLAIDIS, P. & POUILLIKAS, A. 2017 A comparative overview of hydrogen production processes. *Renew. Sust. Energy Rev.* **67**, 597–611.
- NOVEV, J.K. & COMPTON, R.G. 2018 Natural convection effects in electrochemical systems. *Curr. Opin. Electrochem.* **7** (1), 118–129.
- OBATA, K. & ABDI, F. 2021 Bubble-induced convection stabilizes local pH during solar water splitting in neutral pH electrolytes. *Sustain. Energy Fuels* **5** (15), 3791–3801.
- OBATA, K., VAN DE KROL, R., SCHWARZE, M., SCHOMÄCKER, R. & ABDI, F.F. 2020 In situ observation of pH change during water splitting in neutral pH conditions: impact of natural convection driven by buoyancy effects. *Energy Environ. Sci.* **13** (12), 5104–5116.
- OSTILLA-MONICO, R., YANG, Y., VAN DER POEL, E., LOHSE, D. & VERZICCO, R. 2015 A multiple-resolution strategy for direct numerical simulation of scalar turbulence. *J. Comput. Phys.* **301**, 308–321.
- PARK, S., LIU, L., DEMIRKİR, Ç., VAN DER HEIJDEN, O., LOHSE, D., KRUG, D. & KOPER, M.T.M. 2023 Solutal Marangoni effect determines bubble dynamics during electrocatalytic hydrogen evolution. *Nat. Chem.* **15** (11), 1532–1540.
- PROSPERETTI, A. 1982 A generalization of the Rayleigh–Plesset equation of bubble dynamics. *Phys. Fluids* **25** (3), 409–410.
- QIAN, K., CHEN, Z.D. & CHEN, J.J. 1998 Bubble coverage and bubble resistance using cells with horizontal electrode. *J. Appl. Electrochem.* **28** (10), 1141–1145.
- RAMAN, A., PEÑAS, P., VAN DER MEER, D., LOHSE, D., GARDENIERS, H. & FERNÁNDEZ RIVAS, D. 2022 Potential response of single successive constant-current-driven electrolytic hydrogen bubbles spatially separated from the electrode. *Electrochim. Acta* **425** (June), 140691.

- ROUŠAR, I. & CEZNER, V. 1975 Transfer of mass or heat to an electrode in the region of hydrogen evolution – I theory. *Electrochim. Acta* **20** (4), 289–293.
- SAKUMA, G., FUKUNAKA, Y. & MATSUSHIMA, H. 2014 Nucleation and growth of electrolytic gas bubbles under microgravity. *Intl J. Hydrogen Energy* **39** (15), 7638–7645.
- SCHILLINGS, J., DOCHE, O. & DESEURE, J. 2015 Modeling of electrochemically generated bubbly flow under buoyancy-driven and forced convection. *Intl J. Heat Mass Transfer* **85**, 292–299.
- SCHWARZ, S., KEMPE, T. & FRÖHLICH, J. 2015 A temporal discretization scheme to compute the motion of light particles in viscous flows by an immersed boundary method. *J. Comput. Phys.* **281**, 591–613.
- SCRIVEN, L. 1959 On the dynamics of phase growth. *Chem. Engng Sci.* **10** (1–2), 1–13.
- SEPAHI, F., PANDE, N., CHONG, K.L., MUL, G., VERZICCO, R., LOHSE, D., MEI, B.T. & KRUG, D. 2022 The effect of buoyancy driven convection on the growth and dissolution of bubbles on electrodes. *Electrochim. Acta* **403**, 139616.
- SLOOTEN, P. 1984 Departure of vapor- and gas-bubbles in a wide pressure range. PhD thesis, Applied Physics and Science Education.
- SPANDAN, V., MESCHINI, V., OSTILLA-MÓNICO, R., LOHSE, D., QUERZOLI, G., DE TULLIO, M.D. & VERZICCO, R. 2017 A parallel interaction potential approach coupled with the immersed boundary method for fully resolved simulations of deformable interfaces and membranes. *J. Comput. Phys.* **348**, 567–590.
- STEPHAN, K. & VOGT, H. 1979 A model for correlating mass transfer data at gas evolving electrodes. *Electrochim. Acta* **24** (1), 11–18.
- STERNLING, C.V. & SCRIVEN, L.E. 1959 Interfacial turbulence: hydrodynamic instability and the marangoni effect. *AIChE J.* **5** (4), 514–523.
- SWIEGERS, G.F., TERRETT, R.N., TSEKOURAS, G., TSUZUKI, T., PACE, R.J. & STRANGER, R. 2021 The prospects of developing a highly energy-efficient water electrolyser by eliminating or mitigating bubble effects. *Sustain. Energy Fuels* **5** (5), 1280–1310.
- TAKAGI, S. & MATSUMOTO, Y. 2011 Surfactant effects on bubble motion and bubbly flows. *Annu. Rev. Fluid Mech.* **43**, 615–636.
- TAQIEDDIN, A., NAZARI, R., RAJIC, L. & ALSHAWABKEH, A. 2017 Review–physicochemical hydrodynamics of gas bubbles in two phase electrochemical systems. *J. Electrochem. Soc.* **164** (13), E448–E459.
- TORII, K., KODAMA, M. & HIRAI, S. 2021 Three-dimensional coupling numerical simulation of two-phase flow and electrochemical phenomena in alkaline water electrolysis. *Intl J. Hydrogen Energy* **46** (71), 35088–35101.
- TURNER, J.A. 2004 Sustainable hydrogen production. *Science* **305** (5686), 972–974.
- UHLMANN, M. 2005 An immersed boundary method with direct forcing for the simulation of particulate flows. *J. Comput. Phys.* **209** (2), 448–476.
- VANELLA, M. & BALARAS, E. 2009 A moving-least-squares reconstruction for embedded-boundary formulations. *J. Comput. Phys.* **228** (18), 6617–6628.
- VERHAART, H., DE JONGE, R. & VAN STRALEN, S. 1980 Growth rate of a gas bubble during electrolysis in supersaturated liquid. *Intl J. Heat Mass Transfer* **23** (3), 293–299.
- VERZICCO, R. & ORLANDI, P. 1996 A finite-difference scheme for three-dimensional incompressible flows in cylindrical coordinates. *J. Comput. Phys.* **123** (2), 402–414.
- VOGT, H. 1984a The rate of gas evolution at electrodes – 2. An estimate of the efficiency of gas evolution on the basis of bubble growth data. *Electrochim. Acta* **29** (2), 175–180.
- VOGT, H. 1984b The rate of gas evolution of electrodes – 1. An estimate of the efficiency of gas evolution from the supersaturation of electrolyte adjacent to a gas-evolving electrode. *Electrochim. Acta* **29** (2), 167–173.
- VOGT, H. 1989 Mechanisms of mass transfer of dissolved gas from a gas-evolving electrode and their effect on mass transfer coefficient and concentration overpotential. *J. Appl. Electrochem.* **19** (5), 713–719.
- VOGT, H. 2011a On the gas-evolution efficiency of electrodes. 1. Theoretical. *Electrochim. Acta* **56** (3), 1409–1416.
- VOGT, H. 2011b On the gas-evolution efficiency of electrodes. 2. Numerical analysis. *Electrochim. Acta* **56** (5), 2404–2410.
- VOGT, H. 2012 The actual current density of gas-evolving electrodes – Notes on the bubble coverage. *Electrochim. Acta* **78**, 183–187.
- VOGT, H. 2013 On the various types of uncontrolled potential increase in electrochemical reactors–The anode effect. *Electrochim. Acta* **87**, 611–618.
- VOGT, H. 2017 The quantities affecting the bubble coverage of gas-evolving electrodes. *Electrochim. Acta* **235**, 495–499.
- VOGT, H. & BALZER, R.J. 2005 The bubble coverage of gas-evolving electrodes in stagnant electrolytes. *Electrochim. Acta* **50** (10), 2073–2079.

- VOGT, H. & STEPHAN, K. 2015 Local microprocesses at gas-evolving electrodes and their influence on mass transfer. *Electrochim. Acta* **155**, 348–356.
- WESTERHEIDE, D.E. & WESTWATER, J.W. 1961 Isothermal growth of hydrogen bubbles during electrolysis. *AIChE J.* **7** (3), 357–362.
- WHITNEY, G.M. & TOBIAS, C.W. 1988 Mass-transfer effects of bubble streams rising near vertical electrodes. *AIChE J.* **34** (12), 1981–1995.
- WRAGG, A. 1968 Free convection mass transfer at horizontal electrodes. *Electrochim. Acta* **13** (12), 2159–2165.
- YANG, K., KAS, R. & SMITH, W.A. 2019 In situ infrared spectroscopy reveals persistent alkalinity near electrode surfaces during CO₂ electroreduction. *J. Am. Chem. Soc.* **141** (40), 15891–15900.
- YANG, X., BACZYMAŁSKI, D., CIERPKA, C., MUTSCHKE, G. & ECKERT, K. 2018 Marangoni convection at electrogenerated hydrogen bubbles. *Phys. Chem. Chem. Phys.* **20** (17), 11542–11548.
- YANG, X., KARNBACH, F., UHLEMANN, M., ODENBACH, S. & ECKERT, K. 2015 Dynamics of single hydrogen bubbles at a platinum microelectrode. *Langmuir* **31** (29), 8184–8193.
- ZARGHAMI, A., DEEN, N. & VREMAN, A. 2020 CFD modeling of multiphase flow in an alkaline water electrolyzer. *Chem. Engng Sci.* **227**, 115926.
- ZHANG, Z., LIU, W. & FREE, M.L. 2020 Phase-field modeling and simulation of gas bubble coalescence and detachment in a gas-liquid two-phase electrochemical system. *J. Electrochem. Soc.* **167** (1), 013532.
- ZHAO, X., REN, H. & LUO, L. 2019 Gas bubbles in electrochemical gas evolution reactions. *Langmuir* **35** (16), 5392–5408.
- ZUBER, N. 1963 Nucleate boiling. The region of isolated bubbles and the similarity with natural convection. *Intl J. Heat Mass Transfer* **6** (1), 53–78.